

Article

An Overall Linearized Modeling Method and Associated Delay Time Model for the PV System

Xianping Zhu , Shaowu Li * and Jingxun Fan 

College of Intelligent Systems Science and Engineering, Hubei Minzu University, Enshi 445000, China; zxp17873436515@163.com (X.Z.); jingxun_fan@163.com (J.F.)

* Correspondence: xidu_surfer@163.com; Tel.: +86-139-9779-9701

Abstract: There are some significant nonlinearity and delay issues in photovoltaic (PV) system circuits. Therefore, it is very difficult for the existing classic linear control theories to be used in PV systems; this hinders the design of the optimal energy dispatch by considering real-time generation power forecasting methods. To solve this problem, an overall linearized model with variable weather parameters (OLM-VWP) of the PV system is proposed on the basis of small-signal modeling. Meanwhile, a corresponding simplified overall linearized model with variable weather parameters (SOLM-VWP) is presented. The SOLM-VWP avoids analyzing delay characteristics of the complex high-order PV system. Moreover, it can reduce hardware cost and computation time, which makes analysis of the transient performance index of the PV system more convenient. In addition, on the basis of the OLM-VWP and SOLM-VWP, a delay-time model with variable weather parameters (DTM-VWP) of the PV system is also proposed. The delay time of the system can be accurately calculated using the DTM-VWP, and it provides a preliminary theoretical basis for carrying out real-time energy scheduling of the PV system. Finally, simulations are implemented using the MATLAB tool, and experiments are conducted. The results verify that the proposed linearization model of the PV system is accurate and reasonable under varying irradiance and temperature conditions. Meanwhile, the results also verify that the proposed SOLM-VWP and DTM-VWP of the PV system are feasible. Additionally, the results show that some transient performance indexes (delay time, rise time, settling time, and peak time) can be solved by means of equations when the circuit parameters and real-time weather parameters are given.



Citation: Zhu, X.; Li, S.; Fan, J. An Overall Linearized Modeling Method and Associated Delay Time Model for the PV System. *Energies* **2023**, *16*, 4202. <https://doi.org/10.3390/en16104202>

Academic Editor: Philippe Leclère

Received: 10 April 2023

Revised: 14 May 2023

Accepted: 17 May 2023

Published: 19 May 2023



Copyright: © 2023 by the authors. Licensee MDPI, Basel, Switzerland. This article is an open access article distributed under the terms and conditions of the Creative Commons Attribution (CC BY) license (<https://creativecommons.org/licenses/by/4.0/>).

Keywords: photovoltaic system; small-signal modeling; overall linearization; delay-time model

1. Introduction

As the proportion of the PV system continues to increase, grid-connected PV systems are expected to reduce the effective system inertia due to the lack of inertia in large-scale PV generation [1,2]. In a reduced-inertia power system, the active balance is usually disrupted by large and random weather changes following PV generation. To date, many research efforts have been conducted in this area. The use of accurate PV power prediction for dispatch control is considered an important means to effectively solve the above problem. Therefore, it is crucial to accurately develop the DTM-VWP of the PV system to solve problems related to grid dispatch. To obtain this model, however, it is necessary to build a linear model of the overall association. The PV system is a strongly nonlinear system that cannot be studied and analyzed using classic linear control theory. Therefore, the proposed OLM-VWP must completely remove obstacles to using linear theory to analyze these systems. To date, much work has been reported in the literature on linearized modeling, which mainly includes linearized modeling of DC/DC, DC/AC, and PV cells. The current mainstream methods for modeling DC/DC include the description function method, the switching network averaging modeling method, and the state-space averaging method. To improve the accuracy of DC/DC stability analysis, Refs. [3,4] have

proposed the description function method to model the linearization of the switching process in DC/DC. The descriptive function method cannot linearize the modeling of DC/DC containing nonlinear links. To address this limitation, Refs. [5–7] have proposed the linearized modeling method for switching network averaging. In addition, the well-known state-space averaging method has been proposed, which is simple and easy to use for steady-state and small-signal analysis of DC/DC [8]. This state-space averaging method provides important guidelines for DC/DC operation in low-frequency small-signal analysis. The main DC/AC modeling methods are the D-Q small-signal method, the generalized averaging method, and the traditional state-space averaging method [9]. In weak grid conditions, changes in PLL bandwidth may cause the inverter system to lose stability. To overcome this drawback, Refs. [9–11] have proposed the small-signal linearized circuit model for the grid-connected inverter power stage in the system D-Q framework. The D-Q small-signal linearization modeling methods have limitations such as low accuracy and long simulation application time; in contrast, Refs. [12,13] have proposed a generalized averaging linearization model for single-phase and three-phase pulse-width modulated inverters. Modeling based on the generalized averaging method takes into account effects of different parameters, such as amplitude modulation ratio, dead time, and switching frequency. This method ensures accurate estimation of the fundamental components of voltage and current and improves the computational efficiency of the inverter simulation. However, the traditional state-space averaging method used in previous studies still has irreplaceable advantages in low- and medium-frequency systems [14–16]. First, it can be implemented simply and with clear physical meaning. Second, it can improve the stability of the system by analyzing the eigenvalues of the state-space matrix. Finally, it can be further simplified to a reduced-order model by removing states that are irrelevant to the specific stability problem. A large number of contributions have been made by previous researchers in modeling the linearization of DC/DC and DC/AC, but an important obstacle to the overall linearization of the PV system is the linearization of PV cells. These cells exhibit strong nonlinearity as affected by irradiance and temperature. The main methods used to build the linearization model of PV cells are the segmental linearization method and small-signal linearization method. In Ref. [17], a new, explicit mathematical model is proposed using the segmented linearization method to represent the expression of the $I - V$ relationship for the conventional two-diode model of the PV cell. To improve the real-time accuracy of PV MPPT under nonuniform conditions, a new segmented linear model is proposed [18] for the fast and accurate real-time simulation of the PV cell. To simplify the linearized model to a greater extent, Ref. [19] has derived the algebraic equation for the PV cell model using the Taylor approximation in conjunction with traditionally segmented linearization. However, the segmented linearization modeling method has limitations such as computational complexity and MPP inaccuracy. Therefore, most researchers have linearized the modeling of PV cells operating at the MPP. In Ref. [20], researchers proposed equating the diode in the single-diode circuit model to a series connection of resistance and capacitance at the MPP, and the original circuit is equated to Thevenin's equivalent circuit. On the other hand, Ref. [21] has established a linearized model of weather parameters and the external equivalence of the PV cell, and the model included a functional relationship between the MPPT control parameters and the weather, providing a convenient way to implement MPPT. However, previous research has not linearized the overall PV system, and, in particular, no explicit mathematical model is available for the study and analysis of the overall PV system. This drawback prevents the use of classic linear control theory to easily analyze the characteristics of PV systems. Moreover, it is not possible to find the delay time of the system using classic control theory. The DC-side linearization model and OLM-VWP of the PV system are first proposed by modeling the overall PV system with a small signal under input-to-output conditions and control-to-output conditions. These results provide a favorable theoretical basis for the analysis of delay characteristics, the development of energy scheduling strategies, and the selection of control methods. One

of the main objectives and contributions is to obtain DC-side linearization models and OLM-VWP of the PV system.

Another purpose of proposing the linearized mathematical model is to simplify the complex higher-order model of the PV system by using the reduced-order method. It is very difficult to directly study the transient characteristics of a PV system with inverters. For this reason, previous studies have aimed to mathematically model the DC/DC or the DC/AC of the PV system separately [22–24]. These studies have reduced the fourth-order primal systems to second-order models by using functional approximation so that the simplified systems retain the basic characteristics of the primal systems. These studies do not focus on the overall PV system reduced-order model. On this basis, Ref. [25] has divided the overall PV system into two simplified linearized models for research and analysis to address the analysis of low-frequency oscillations. The research of [26] has concluded that the reduced-order model of the DC-side microgeneration system is not applicable to the AC system. In Ref. [27], a small-signal model for inverter-based microgrids with reduced order is proposed, and the microgrid system is simplified using the singular ingestion algorithm. The linearized mathematical models as proposed in Refs. [25–27] are still matrix equations of higher order, which cannot be directly calculated using the classic linear control theory to analyze the PV system. These models are still time-consuming and have a large computational burden when using linear control theory in time-domain analysis. Especially for applications related to real-time scheduling control by calculating delay times and transient characteristics, the existing linearized models still lack engineering practicality. Therefore, the OLM-VWP is further developed for simplified modeling. To remedy this deficiency, this paper uses the simplified OLM-VWP based on the Routh approximation reduced-order method. On the one hand, the transient characteristics of the analyzed PV system are solved more easily using this model based on real-time values of irradiance and temperature. On the other hand, it is easy to analyze the steady-state performance of the PV system based on this model. The proposed SOLM-VWP of the PV system is crucial in developing the DTM-VWP of the PV system and developing a control strategy for real-time energy dispatch of the PV system. The SLOM can avoid computational complexity in its scheduling controller, making the hardware (especially the microprocessor) less expensive and the computation time shorter. This work plays an important role in engineering applications for the PV system.

Delays in a PV system can affect system stability. For example, in Ref. [28], the inverter delay was found to affect the harmonic characteristics of a grid-connected large PV system; in Ref. [29], the introduction of a digital time delay increased the system steady-state error; and in Ref. [30], the system time-lag limited the performance of the active damping method. Researchers in [31] investigated the delay time of three different DC/DC systems for a comparative analysis of the transient response due to lightning strikes. Researchers in [32] studied MPPT under partial shading conditions, where delay parameters affected PV system security and electrical faults, as well as output power and operating point variations [33]. To ensure voltage stability of the distribution network, the power compensation control of the PV system is based on the delay parameter. The delay-tolerant predictive power compensation control for distribution feeder voltage regulation is proposed in Ref. [34]. Moreover, Refs. [28,35] have performed small-signal modeling of the PV system and discussed the effect of delay time on dynamic and steady-state performance. The abovementioned studies generally have focused on delay time affecting the PV system and have provided many methods to compensate for the associated impact. However, few mathematical expressions for the DTM-VWP of PV systems have been reported. Therefore, it is impossible to calculate the delay time of the PV system. These problems also hinder the optimal control of these systems in real time. To solve this problem, the DTM-VWP for the PV system is proposed based on the SOLM-VWP. The relationships between irradiance, temperature, and circuit parameters have been proposed in some VWP methods [36–38]. These transient performances (delay time and output power) of the PV system can be calculated using these methods in advance. This method provides the prior theoretical

basis for implementing a real-time, predictive control energy scheduling method and carrying out an active energy scheduling method. Obviously, using the linearized DTM-VWP to solve the scheduling control problem is very different from other existing problems that involve solving scheduling control strategies, which is one of the main contributions and innovations of the present work.

The main innovations and contributions of this work can be illustrated as follows:

- (1) A new method for modeling the overall linearization of the PV system is proposed.
- (2) A first attempt is made to study the PV system DTM-VWP by solving for S and T .
- (3) An SOLM-VWP of the PV system containing a reduced-order model is proposed.
- (4) The t_d and output characteristic of the PV system can be solved directly using S and T .
- (5) Through this work, v_o of the PV system can be predicted using t_d of the PV system.

The paper is divided into the following sections. In Section 2.1, based on the small-signal modeling of each unit of the PV system, it is proposed that from the input $c(S, T)$ or control $d(S, T)$ to the DC-side output v_o and OLM-VWP, respectively. In Section 2.2, the OLM-VWP of the PV system is presented so that the system can be analyzed using classic linear control theory. In Section 2.3, the proposed SOLM-VWP is based on the OLM-VWP of the PV system. The main purpose is to improve the engineering practicality of the OLM-VWP and to provide a theoretical basis for modeling the DTM-VWP of the PV system. The OLM-VWP is reduced in order using the Routh approximation method to derive its SOLM-VWP. In Section 2.4, the delay time t_d and output transient performance of the system are investigated by linearizing the model using classic linear control theory, and the DTM-VWP of the system is further proposed. In Section 3, the input $c(S, T)$ to output the v_o small-signal linearization model and the control variable $d(S, T)$ to output the v_o small-signal linearization model and its simplified model are simulated and validated against actual circuits. The dynamic performance of the higher-order linearization model and that of the simplified second-order model are compared and analyzed. In addition, the proposed DTM-VWP is validated in conjunction with experiments to verify the accuracy and validity of the model. In Sections 4 and 5, some important conclusions are separately analyzed and summarized.

2. Materials and Methods

2.1. The Small-Signal Model for the PV System

2.1.1. Circuit Model of the PV System

Before modeling the PV system circuit, some assumptions are given. (1) The PV system is always near the MPP at a steady state. (2) The sampled S and T values measured using the sensors must be accurate and obtained in real time. The VWP-MPPT control method [38] is applied for maximum power tracking, and the block diagram of the PV system composition is displayed in Figure 1. The main circuit mainly consists of the PV cell, DC/DC, DC/AC, digital controller, and grid connection or load. The digital controller is mainly used to acquire the S and T of the PV cell and the voltage and current of the inverter output, and to drive DC/DC for MPPT and DC/AC for grid-connected operation. There are three main basic topologies of DC/DC in the PV system [39]: Buck circuit, Boost circuit, and Buck–Boost circuit. Figure 2 is used as the object of study for the PV system. The study establishes the OLM-VWP of the whole system, which is theoretically based on the small-signal linearized mathematical model of the PV cell, DC/DC, DC/AC, and digital controller.

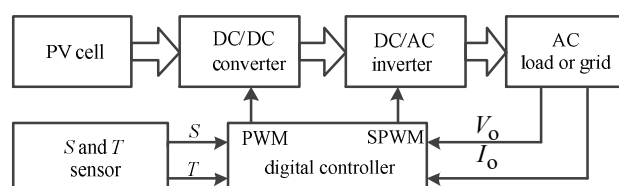


Figure 1. Block diagram of the PV system composition.

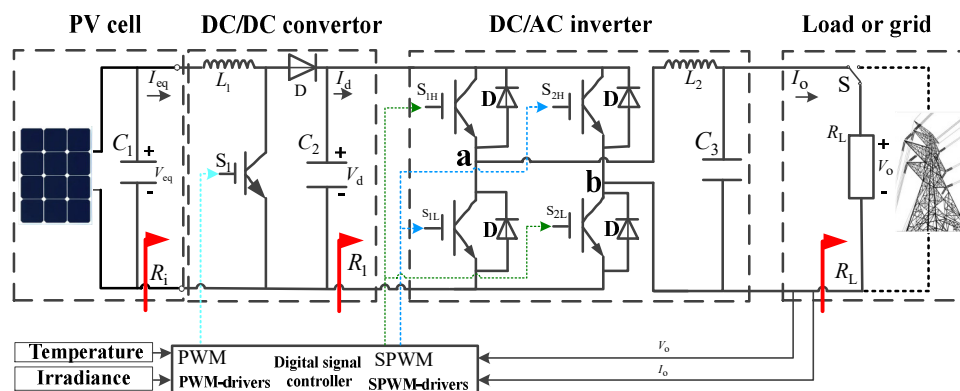


Figure 2. Structure of the PV system with the PV-Boost circuit structure.

2.1.2. The dc-Side linearization Models of the PV System

The mathematical model of the PV cell is expressed using Equation (1) [37], which is simulated using MATLAB simulation software (Version 2019), and the corresponding $I - V$ curves are shown in Figure 3.

$$I = I_L - I_0 \left[e^{\frac{q(V+IR_s)}{AKT}} - 1 \right] - \frac{V_{eq} + IR_s}{R_{sh}} \tag{1}$$

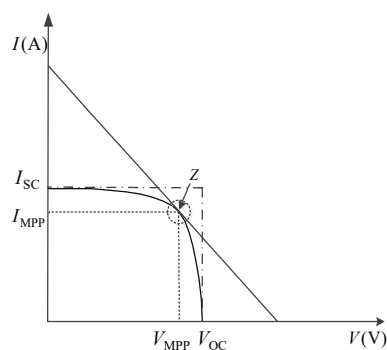


Figure 3. Linear equivalence principle of PV cells.

To establish the mathematical model of the PV system, it is necessary to linearize the PV cell response. The PV system can be linearized when a tangent is applied to the $I - V$ curve at the MPP [37] to simplify the equivalent model into the Thevenin equivalent circuit model. To ensure that the PV system operates under continuous current conditions, the characteristic that the cell is capacitive on the generation side is also considered. Therefore, an equivalent substitution is made by connecting a capacitor in parallel to the equivalent circuit of the cell. The equivalent circuit model can be obtained as shown in Figure 4. Equations (2) and (3) apply when the PV system is operating at the MPP; based on these, the corresponding transfer function of the equivalent cell circuit is obtained as Equation (4). The value of the parameter $C(S, T)$ is related to the PV cell itself and to S and T of the weather conditions in Equation (3).

$$R_{eq} = R_i = \frac{V_{MPP}}{I_{MPP}} \tag{2}$$

$$V_{SM} = 2V_{MPP} = 2C(S, T) \tag{3}$$

$$G_1(s) = \frac{V_{eq}}{V_{SM}} = \frac{V_{eq}}{2C(S, T)} = \frac{1}{R_{eq}C_1s + 1} \tag{4}$$

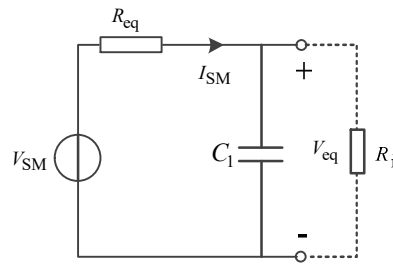


Figure 4. Linear equivalence circuit of the PV cell.

The nonlinear components of DC/DC include power switching devices and diodes and are thus nonlinear circuits. When DC/DC runs near a certain steady-state operating point, the small-signal perturbations can be linearized using the state-space averaging method. Then, DC/DC can be described using the transfer function. When the system at the MPP is established as equal D and $D_{max}(S, T)$, the maximum power is P_{max} [38,40]. $D_{max}(S, T)$ can be expressed using curve fitting as a function of S and T . The corresponding mathematical models of $D_{max}(S, T)$ for the three basic DC/DC (Buck circuit, Boost circuit, and Buck–Boost circuit) are shown in Equations (5)–(7), respectively. Thus, the relationship between the duty cycles $D_{max}(S, T)$, S , and T is established, where D_M is the abbreviated form of $D_{max}(S, T)$.

$$D_M = D_{max}(S, T) = \frac{\sqrt{P_{max}(S, T)R_1}}{C(S, T)} \tag{5}$$

$$D_M = D_{max}(S, T) = 1 - \frac{C(S, T)}{\sqrt{P_{max}(S, T)R_1}} \tag{6}$$

$$D_M = D_{max}(S, T) = 1 - \frac{C(S, T)}{C(S, T) + \sqrt{P_{max}(S, T)R_1}} \tag{7}$$

The DC-side linearization model of the PV system from input-to-output for the PV-Buck circuit, PV-Boost circuit, and PV-Buck–Boost circuit structures can be represented using Equations (8)–(10), respectively. These equations are derived from the small-signal model of DC/DC and Equation (4) in conjunction with Equations (5)–(7).

$$G_2(s) = \left. \frac{v_d(s)}{c(S, T)(s)} \right|_{d(S, T)(s)=0} = \frac{2D_M}{\left(L_1 C_2 s^2 + \frac{L_1}{R_1} s + 1 \right) (R_{eq} C_1 s + 1)} \tag{8}$$

$$G_3(s) = \left. \frac{v_d(s)}{c(S, T)(s)} \right|_{d(S, T)(s)=0} = \frac{2(1 - D_M)}{\left(L_1 C_2 s^2 + \frac{L_1}{R_1} s + (1 - D_M)^2 \right) (R_{eq} C_1 s + 1)} \tag{9}$$

$$G_4(s) = \left. \frac{v_d(s)}{c(S, T)(s)} \right|_{d(S, T)(s)=0} = \frac{-2D_M(1 - D_M)}{\left(L_1 C_2 s^2 + \frac{L_1}{R_1} s + (1 - D_M)^2 \right) (R_{eq} C_1 s + 1)} \tag{10}$$

Similarly, the DC-side linearization model of the PV system from control to output for the PV-Buck circuit, PV-Boost circuit, and PV-Buck–Boost circuit structures can be represented using Equations (11)–(13), respectively. These equations are derived from the small-signal model of the DC/DC and Equation (4) in conjunction with Equations (5)–(7).

$$G_5(s) = \left. \frac{v_d(s)}{d(S, T)(s)} \right|_{c(S, T)(s)=0} = \frac{2C(S, T)}{\left(L_1 C_2 s^2 + \frac{L_1}{R_1} s + 1 \right) (R_{eq} C_1 s + 1)} \tag{11}$$

$$G_6(s) = \left. \frac{v_d(s)}{d(S, T)(s)} \right|_{c(S, T)(s)=0} = \frac{2C(S, T) \left(1 - \frac{L_1}{(1 - D_M)^2 R_1} s \right)}{\left(L_1 C_2 s^2 + \frac{L_1}{R_1} s + (1 - D_M)^2 \right) (R_{eq} C_1 s + 1)} \tag{12}$$

$$G_7(s) = \frac{v_d(s)}{d(S, T)(s)} \Big|_{c(s, T)(s)=0} = \frac{2C(S, T) \left(\frac{L_1 D_M}{(1-D_M)^2 R_1} s - 1 \right)}{\left(L_1 C_2 s^2 + \frac{L_1}{R_1} s + (1-D_M)^2 \right) (R_{eq} C_1 s + 1)} \quad (13)$$

2.1.3. The Linearization Model of the DC/AC

When analyzing DC/AC, the state-space averaging method used in this paper is the linear model. The switching states are not continuous during the DC/AC circuit operation. The topology diagram of the single-phase full-bridge inverter is shown in Figure 2. The transfer function G_8 is shown in Equation (14). In the DC/AC system using the SPWM control method [41], V_{tri} is usually set as 1, and V_m is equal to the proportionality factor K_{pwm} so that the modulation ratio M in the SPWM control method is equal to K_{pwm} . This mathematical relationship is expressed in Equation (15).

$$G_8(s) = \frac{V_o}{V_d} = \frac{K_{pwm}}{L_2 C_3 s^2 + \left(\frac{L_2}{R_L} + r C_3 \right) s + 1 + \frac{r}{R_L}} \quad (14)$$

When the equivalent series inductor r during filtering is ignored, Equations (14) and (15) can be reduced to Equation (16).

$$K_{pwm} = M = \frac{V_o(s)}{V_d(s)} = \frac{V_m}{V_{tri}} \quad (15)$$

$$G_9(s) = \frac{V_o}{V_d} = \frac{M}{L_2 C_3 s^2 + \frac{L_2}{R_L} s + 1} \quad (16)$$

2.1.4. Linearized Modeling for the PV System Controller's Delay Time

In PV power control systems, different structures of digital controllers operate discretely, which increases the control system delay time [42,43]. The total delay time comprises the delay time in the sampling period of the microcontroller, the delay time in the calculation cycle of the A/D converter, and the delay time in PWM control. The mathematical expression of these delay times is shown using Equation (17). This equation can also be reduced to Equation (18), where T_s refers to the sampling period.

$$G_{10}(s) = \frac{e^{T_s s} (1 - e^{T_s s})}{T_s s} \quad (17)$$

$$G_{10} \approx G_{11}(s) = \frac{1}{T_d s + 1} \quad (18)$$

In the PV control system, the delay time T_d of the controller is set to 1.5 times the sampling period T_s . Therefore, the transfer function of the delay link can be expressed as in Equation (19).

$$G_{12}(s) = e^{-T_d s} \quad (19)$$

2.2. The OLM-VWP of the PV System

According to the theory of PV cell linearization in Section 2.1.2, the PV cell can be linearized only when the PV system operates at the MPP. However, the necessary condition is that R_{eq} equals R_i to make the PV system MPPT. In the actual PV system, the DC/DC is controlled using the digital signal controller. In this way, these converters perform MPPT by changing the final R_i to R_{eq} [37]. Before analyzing the OLM-VWP of the PV system, the following assumptions are made about the circuit structure of Figure 2:

- (1) All circuit components in the circuit are ideal components.

- (2) The capacity values of the inductor and capacitor of the DC/DC are set to larger values to ensure that the DC/DC operates in continuous mode.
- (3) The PV system is always controlled at the MPP.

First, according to Figure 2, Equations (20)–(23) are established based on the power balance relationship and the circuit theorem.

$$V_{eq}I_{eq} = V_dI_d = V_oI_o \tag{20}$$

$$R_i = \frac{V_{eq}}{I_{eq}} \tag{21}$$

$$R_1 = \frac{V_d}{I_d} \tag{22}$$

$$R_L = \frac{V_o}{I_o} \tag{23}$$

In a PV cell equivalent circuit, three different DC/DCs, DC/ACs, and digital controllers constitute the PV system. These circuit parameters are shown in Table 1. The OLM-VWP of the PV system can be derived from Equations (24)–(26) and Table 1.

$$V_o = \frac{MV_{eq}}{\sqrt{2}} \tag{24}$$

$$R_1 = \frac{2R_L}{M^2} \tag{25}$$

$$P_M = \sqrt{P_{max}(S, T) \frac{2R_L}{M^2}} \tag{26}$$

D_M is the duty cycle at the MPP, and $P_{max}(S, T)$ is the maximum power. The mathematical relationship between $P_{max}(S, T)$ and S, T can be expressed using Equation (27). The mathematical relationship between $C(S, T)$ and S, T can be expressed using Equation (28).

$$P_{max}(S, T) = \begin{cases} 11.772 \times 10^{-8}S^3 - 11.968 \times 10^{-5}S^2 \\ +0.5986S + 10.656 - 0.18T & 0 \leq T \leq 40 \\ 11.772 \times 10^{-8}S^3 - 11.968 \times 10^{-5}S^2 \\ +0.5988S + 10.656 & -20 \leq T \leq 0 \end{cases} \tag{27}$$

$$C(S, T) = 18.48 \times 10^{-6} \times (S - 638.25)^2 + 69.148 \\ + (25 - T) \times 2.064 \tag{28}$$

Table 1. Circuit parameters of differently structured PV systems.

Structure of Different PV Systems	PV-Buck	PV-Boost	PV-Buck–Boost
D_M	$\frac{P_M}{C(S, T)}$	$1 - \frac{C(S, T)}{P_M}$	$1 - \frac{C(S, T)}{C(S, T) + P_M}$
R_i	$\frac{1}{D^2} \frac{2R_L}{M^2}$	$(1 - D)^2 \frac{2R_L}{M^2}$	$\frac{(1 - D)^2 2R_L}{D^2 \frac{2R_L}{M^2}}$
V_d	DV_{eq}	$\frac{V_{eq}}{1 - D}$	$\frac{DV_{eq}}{1 - D}$

Then, when the Buck circuit is used as the DC/DC of the PV system, the structure of the PV system is the PV-Buck circuit. The OLM-VWP of the PV-Buck structure

from input-to-output can be represented using Equation (29), derived by combining Equations (4), (8), (16), (19), (27) and (28).

$$G_{13}(s) = \frac{v_o(s)}{c(S, T)(s)} \Big|_{d(S, T)(s)=0} = \frac{2D_M G_{12} G_9}{\left(\frac{2C_1 R_L}{M^2 (D_M)^2} s + 1 \right) \left(L_1 C_2 s^2 + \frac{M^2 L_1}{2R_L} s + 1 \right)} \quad (29)$$

Similarly, when the Boost circuit is used as the DC/DC of the PV system, the structure of the PV system is the PV-Boost circuit. The OLM-VWP of the PV-Boost circuit structure from input-to-output can be represented using Equation (30), derived by combining Equations (4), (9), (16), (19), (27) and (28).

$$G_{14}(s) = \frac{v_o(s)}{c(S, T)(s)} \Big|_{d(S, T)(s)=0} = \frac{-2D_M(1 - D_M) G_{12} G_9}{\left(\frac{2R_L(1 - D_M)^2 C_1}{M^2 (D_M)^2} s + 1 \right) \left(L_1 C_2 s^2 + \frac{M^2 L_1}{2R_L} s + (1 - D_M)^2 \right)} \quad (30)$$

Similarly, when the Buck-Boost circuit is used as the DC/DC of the PV system, the structure of the PV system is the PV-Buck-Boost circuit. The OLM-VWP of the PV-Buck-Boost circuit structure from input-to-output can be represented using Equation (31), derived by combining Equations (4), (10), (16), (19), (27) and (28).

$$G_{15}(s) = \frac{v_o(s)}{c(S, T)(s)} \Big|_{d(S, T)(s)=0} = \frac{-2D_M(1 - D_M) G_{12} G_9}{\left(\frac{2R_L(1 - D_M)^2 C_1}{M^2 (D_M)^2} s + 1 \right) \left(L_1 C_2 s^2 + \frac{M^2 L_1}{2R_L} s + (1 - D_M)^2 \right)} \quad (31)$$

Similarly, the OLM-VWP of the PV-Buck circuit structure from control-to-output can be represented using Equation (32), derived by combining Equations (4), (11), (16), (19), (27) and (28).

$$G_{16}(s) = \frac{v_o(s)}{d(S, T)(s)} \Big|_{c(S, T)(s)=0} = \frac{2C(S, T) G_{12} G_9}{\left(\frac{2C_1 R_L}{M^2 (D_M)^2} s + 1 \right) \left(L_1 C_2 s^2 + \frac{M^2 L_1}{2R_L} s + 1 \right)} \quad (32)$$

Similarly, the OLM-VWP of the PV-Boost circuit structure from control-to-output can be represented using Equation (33), derived by combining Equations (4), (12), (16), (19), (27) and (28).

$$G_{17}(s) = \frac{v_o(s)}{d(S, T)(s)} \Big|_{c(S, T)(s)=0} = \frac{2C(S, T) \left(1 - \frac{M^2 L_1}{2(1 - D_M)^2 R_L} s \right) G_{12} G_9}{\left(\frac{2(1 - D_M)^2 C_1 R_L}{M^2} s + 1 \right) \left(L_1 C_2 s^2 + \frac{M^2 L_1}{2R_L} s + (1 - D_M)^2 \right)} \quad (33)$$

Finally, the OLM-VWP of the PV-Buck-Boost circuit structure from control-to-output can be represented using Equation (34), derived by combining Equations (4), (13), (16), (19), (27) and (28).

$$G_{18}(s) = \frac{v_o(s)}{d(S, T)(s)} \Big|_{c(S, T)(s)=0} = \frac{2C(S, T) \left(\frac{D_M M^2 L_1}{2(1 - D_M)^2 R_L} s - 1 \right) G_{12} G_9}{\left(\frac{2(1 - D_M)^2 C_1 R_L}{M^2 (D_M)^2} s + 1 \right) \left(L_1 C_2 s^2 + \frac{M^2 L_1}{2R_L} s + (1 - D_M)^2 \right)} \quad (34)$$

2.3. The OLM-VWP of Order Reduction

The SOLM-VWP of the PV system is proposed by reducing the higher-order system of Equations (29)–(34) to the second-order system. The first reason is that the SOLM-VWP is proposed as a prerequisite to subsequently solving the DTM-VWP. The second reason is to reduce the analysis complexity of the output transient characteristics of the PV system. The third reason is to augment the practicality and effectiveness of the OLM-VWP for the PV systems in engineering practice. Note that the complex higher-order OLM-VWP can be simplified using the proposed improved Routh approximation method [43]. This method can fill the gap in many higher-order systems where the traditional dominant

pole method is not applicable. There is no dominant pole in the unit negative feedback system of the OLM-VWP of the PV system. For example, the unit negative feedback of Equation (29) is shown in Figure 5. The SOLM-VWP of the PV system is proposed using the Routh approximation, which requires solving two parameter tables, namely, the alpha table (α -table) and the beta table (β -table). In these tables, the process of computing the parameters in the α -table is as easy as computing the parameters of the Routh–Hurwitz table [44]. However, the process of solving for the parameters in the β -table is much more complicated than that of the α -table. To avoid the complicated computer procedure associated with the α and β -tables, a mathematical model based on the Routh approximation is proposed to reduce the sixth-order transfer function of Equation (35) to the second-order Equation (43). This model retains the low- and medium-frequency characteristics when $e^{-T_d s}$ in Equation (29) is replaced by Equation (18) to better carry out the higher-order model simplified calculation. Similarly, the OLM-VWP of the PV system in Equations (29)–(34) constitutes the degraded reduction of this method, and the SOLM-VWP does not lose the important control characteristics of the original higher-order system. After successful order reduction, the typical second-order system provides more convenience for studying the DTM-VWP theory of the PV system. Equations (35)–(43) provide the reduced-order model for the OLM of the PV-Buck circuit structure. For additional structures of the oversized linear models, the reduced-order methods are calculated accordingly.

$$G(s) = \frac{v_o(s)}{c(S, T)(s)} \Big|_{d(S, T)(s)=0} = \frac{B_0 s + B_1}{A_0 s^6 + A_1 s^5 + A_2 s^4 + A_3 s^3 + A_4 s^2 + A_5 s + A_6} \tag{35}$$

$$A_0 = \frac{2C_1 C_2 C_3 L_1 L_2 R_L T_d}{(D_M)^2 M^2} \tag{36}$$

$$A_1 = \frac{L_1 L_2 \left(C_2 C_3 T_d (D_M)^2 M^2 + C_1 C_3 T_d M^2 + 2C_1 C_2 T_d + 2C_1 C_2 C_3 R_L \right)}{(D_M)^2 M^2} \tag{37}$$

$$A_2 = \frac{\left(\begin{aligned} &4C_1 C_2 L_1 R_L^2 T_d + 4C_1 C_3 L_2 R_L^2 T_d + \\ &2C_1 L_1 L_2 M^4 T_d + 4C_1 C_2 L_1 L_2 R_L + \\ &2C_1 C_3 L_1 L_2 M^2 R_L + 2C_2 (D_M)^2 \\ &L_1 L_2 M^2 T_d + C_3 (D_M)^2 L_1 L_2 M^4 T_d + \\ &2C_2 C_3 (D_M)^2 L_1 L_2 M^2 R_L \end{aligned} \right)}{2(D_M)^2 M^2 R_L} \tag{38}$$

$$A_3 = \frac{\left(\begin{aligned} &4C_1 C_2 L_1 R_L^2 T_d + 4C_1 C_3 L_2 R_L^2 T_d + \\ &2C_1 L_1 L_2 M^4 T_d + 4C_1 C_2 L_1 L_2 R_L + \\ &2C_1 C_3 L_1 L_2 M^2 R_L + 2C_2 (D_M)^2 \\ &L_1 L_2 M^2 T_d + C_3 (D_M)^2 L_1 L_2 M^4 T_d \\ &+ 2C_2 C_3 (D_M)^2 L_1 L_2 M^2 R_L \end{aligned} \right)}{2(D_M)^2 M^2 R_L} \tag{39}$$

$$A_4 = \left(\begin{aligned} &\left(\frac{L_2}{R_L} + \frac{L_1 M^2}{2R_L} + \frac{2C_1 R_L}{(D_M)^2 M^2} \right) T_d \\ &+ \frac{C_1 L_1}{(D_M)^2} + \frac{2C_1 L_2}{(D_M)^2 M^2} + \frac{L_1 L_2 M^2}{2R_L^2} \\ &+ C_2 L_1 + C_3 L_2 \end{aligned} \right) \tag{40}$$

$$A_5 = T_d + \frac{L_2}{R_L} + \frac{L_1 M^2}{2R_L} + \frac{2C_1 R_L}{(D_M)^2 M^2} \tag{41}$$

$$\begin{cases} A_6 = 1 \\ B_0 = 0 \\ B_1 = 2(D_M)M \end{cases} \tag{42}$$

$$\begin{cases} G(s) = \frac{\frac{B_0}{F}s + \frac{B_1}{F}}{s^2 + \frac{A_5}{F}s + \frac{A_6F}{A_5}} \\ F = \left(A_4 - A_6 \times \frac{A_3}{A_5} \right) \end{cases} \quad (43)$$

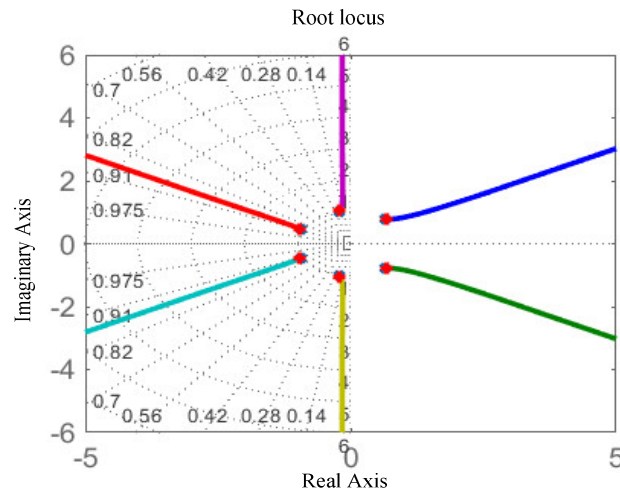


Figure 5. Global linearized model root locus of the unit negative feedback PV-Buck circuit structure.

2.4. The DTM-VWP of the PV System

The OLM-VWP and SOLM-VWP of the PV system are proposed in the preceding section. These results provide the theoretical basis for solving the DTM-VWP of the PV system. The DTM-VWP is used to analyze the relationship between the output and the delay time of the system, as well as its transient characteristics. The algorithm that solves the DTM-VWP of the PV system is shown below. First, the small-disturbance signal inputs for the OLM-VWP are $c(S, T)$ or $d(S, T)$. The OLM-VWP of the PV-Buck circuit, PV-Boost circuit, and PV-Buck-Boost circuit structures are represented using Equations (29)–(34), respectively. Based on this, the SOLM-VWP is derived by reducing the order of the OLM-VWP. Then, based on the SOLM-VWP, the functional relationship between the output of the PV system and the delay time can be derived from the theoretical method of classic control theory. Finally, the classic linear control theory is used to solve for the delay time of the system with overdamping. The delay time of the PV system is equal to the time that it takes for the system to reach half of its steady-state value for the first time, and its functional relationship is expressed using Equation (44). To derive the time required for v_t , the SOLM-VWP is fitted to the curve function, which solves for the delay time t_d corresponding to the output of the PV system. The values of $c(S, T)$ and $d(S, T)$ of the SOLM-VWP can be measured, and the circuit parameters and circuit structure are known. The delay time can be calculated directly from Equations (45)–(50).

$$v_t = \frac{v_o}{2} \quad (44)$$

Equation (45) can be derived from the SOLM-VWP model of Equations (43) and (44). It is the DTM-VWP of the PV-Buck circuit in the condition of input perturbation.

$$t(v_t) = \frac{a_1 v_t^2 + a_2 v_t + a_3}{v_t^3 + b_1 v_t^2 + b_2 v_t + b_3} \quad (45)$$

Equation (46) can be derived from the SOLM-VWP model of Equations (43) and (44). It is the DTM-VWP of the PV-Boost circuit in the condition of input perturbation.

$$t(v_t) = \frac{a_1 v_t^2 + a_2 v_t + a_3}{v_t^3 + b_1 v_t^2 + b_2 v_t + b_3} \quad (46)$$

Equation (47) can be derived from the SOLM-VWP model of Equations (43) and (44). It is the DTM-VWP of the PV-Buck–Boost circuit in the condition of input perturbation.

$$t(v_t) = \frac{a_1 v_t^3 + a_2 v_t^2 + a_3 v_t + a_4}{v_t^5 + b_1 v_t^4 + b_2 v_t^3 + b_3 v_t^2 + b_4 v_t + b_5} \quad (47)$$

Equation (48) can be derived from the SOLM-VWP model of Equations (43) and (44). It is the DTM-VWP of the PV-Buck circuit in the condition of control perturbation.

$$t(v_t) = \frac{a_1 v_t^3 + a_2 v_t^2 + a_3 v_t + a_4}{b_1 v_t^4 + b_2 v_t^3 + b_3 v_t^2 + b_4 v_t + b_5} \quad (48)$$

Equation (49) can be derived from the SOLM-VWP model of Equations (43) and (44). It is the DTM-VWP of the PV-Boost circuit in the condition of control perturbation.

$$t(v_t) = \frac{a_1 v_t^4 + a_2 v_t^3 + a_3 v_t^2 + a_4 v_t + a_5}{v_t^5 + b_1 v_t^4 + b_2 v_t^3 + b_3 v_t^2 + b_4 v_t + b_5} \quad (49)$$

Equation (50) can be derived from the SOLM-VWP model of Equations (43) and (44). It is the DTM-VWP of the PV-Buck–Boost circuit in the condition of control perturbation.

$$t(v_t) = \frac{a_1 v_t^4 + a_2 v_t^3 + a_3 v_t^2 + a_4 v_t + a_5}{v_t^5 + b_1 v_t^4 + b_2 v_t^3 + b_3 v_t^2 + b_4 v_t + b_5} \quad (50)$$

Equations (45) and (46) are the DTM-VWP for PV-Buck and PV-Boost under the input perturbation condition, respectively. From the expressions, it can be seen that the functional expressions of Equations (45) and (46) are similar. Similarly, the expressions of Equations (49) and (50) are similar. Although the function expressions are similar, the parameters in their expressions are not the same. This result can also be seen in Section 3.1.4 regarding DTM-VWP.

3. Results

3.1. Simulation Experiments

3.1.1. The OLM-VWP Verification on the DC Side of the PV System

The linearized model for the DC side of the PV system at the MPP is given by Equations (8)–(13). These results provide the theoretical basis for proposing the OLM of the PV system with inverters under the MPP conditions. For this purpose, six sets of simulation experiments are carried out using MATLAB software. The proposed DC-side linearization model is verified by experiments. In these experiments, the PV system is assumed to operate at maximum power at constant irradiance and temperature for the following conditions. For the simulation experiments, the parameters of the PV cell and the circuit are given in Tables 2 and 3, respectively. The DC/DC of the PV system is selected as the Buck circuit, Boost circuit, and Buck–Boost circuit structures for simulation verification.

Table 2. Parameters of the PV cell.

Quantity	Notation	Value
Maximal output power	$P_{\max}/(W)$	150.15
Open-circuit voltage	$V_{OC}/(V)$	22
Short-circuit current	$I_{SC}/(A)$	9.19
Reference temperature	$T_{ref}/(^{\circ}C)$	25
Reference irradiance	$S_{ref}/(W/m^2)$	1000
Output voltage at maximum power	$V_{MPP}/(V)$	17.5
Output current at maximum power	$I_{MPP}/(A)$	8.58
Number of PV cells		4

Table 3. Circuit parameters in the simulation.

Quantity	Notation	Value
Filter capacitors for PV cells	C_1 /(μF)	4.7×10^{-3}
Filter capacitors for DC/DC	C_2 /(μF)	4.7×10^{-3}
Filter capacitor for DC/AC	C_3 /(μF)	2.2×10^{-7}
Power inductors for DC/DC	L_1 /(mH)	4.7×10^{-3}
Filter inductor for DC/AC	L_2 /(mH)	5×10^{-5}
Load resistance	R_L /(Ω)	500
Switching frequency	f_{PWM} /(kHz)	20
Modulation ratio	M	0.5
MOSFET	Internal resistance/(m Ω)	1
MOSFET	Buffer resistance/(k Ω)	500
Diode	Internal resistance/(m Ω)	1
Diode	Buffer resistance/(Ω)	500
Input small disturbance	$c(S, T)$	
Control small disturbances	$d(S, T)$	

To verify whether the OLM-VWP is of greater engineering utility, the experimental data are simulated by choosing data from the actual PV power stations, and these data characteristics are given in Figure 6. The simulation experiment was conducted by selecting three sets of representative data from the one-day operation of the PV system. The experimental results are given in Tables 4 and 5. The experimental results are shown in Figures 7–12.

According to Figures 7–12, in the simulation experiments, the PV system at S and T (400 W/m^2 , 10°C) is operating at the steady state. S and T (1000 W/m^2 , 25°C) represent the perturbed signal inputs. These experiments verify that the DC-side linearization model is feasible and usable. On the one hand, an intuitive analysis of Figures 7–9 indicates that the response characteristics of the DC-side linearization models and the simulated circuit are approximately the same when the VWP is used as an input perturbation. Alternately, Figures 10–12 indicate that the response characteristics of the DC-side linearization model and the simulated circuit are approximately the same when the control variable is used as an input perturbation.

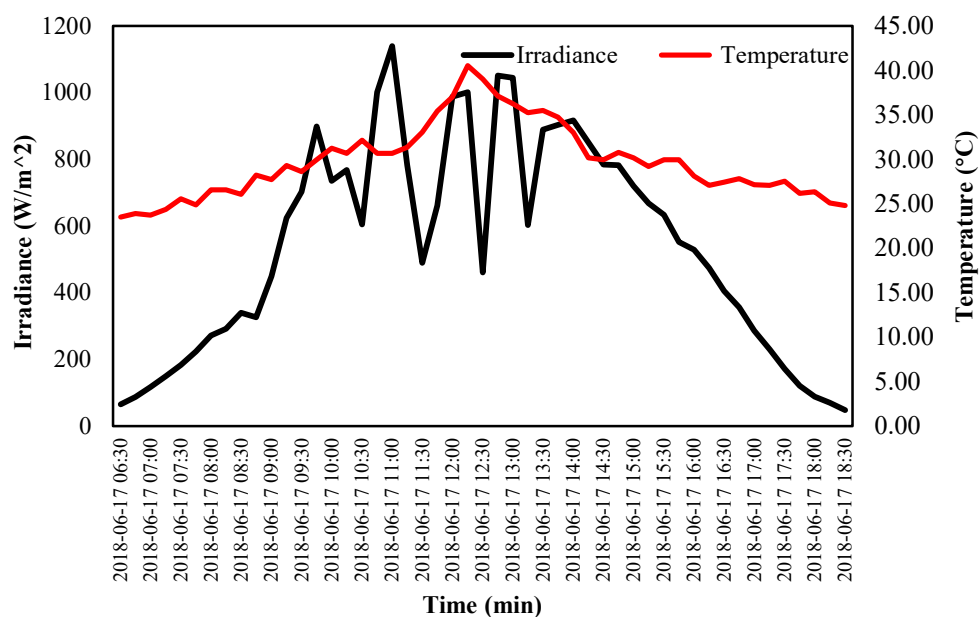
**Figure 6.** Trend diagram of weather parameters of the PV system.

Table 4. Transient performance indexes of the DC/DC input-to-output for the linearized models.

Difference Structure DC/DC	Initial Value Status (S,T)/(W/m ² , °C)	Perturbation Value Status (S,T)/(W/m ² , °C)	$c(S,T)$	$D_{max}(S,T)$	$t_d/(s)$	$t_p/(s)$	$t_r/(s)$	$t_s/(s)$
Buck	400,10	1000,40	4.74	0.425	0.242	0.837	0.483	0.552
	800,30	1000,40	0.78	0.627	0.109	0.449	0.219	0.301
	1000,40	800,10	4.19	0.722	0.071	0.194	0.142	0.155
Boost	400,10	1000,40	4.74	0.256	0.176	0.393	0.351	1.073
	800,30	1000,40	0.78	0.496	0.071	0.214	0.141	1.418
	1000,40	800,10	4.19	0.562	0.074	0.232	0.147	1.586
Buck-Boost	400,10	1000,40	4.74	0.573	0.112	0.288	0.223	1.299
	800,30	1000,40	0.78	0.665	0.099	0.306	0.199	1.597
	1000,40	800,10	4.19	0.695	0.102	0.322	0.203	1.518

Table 5. Transient performance indexes of the DC/DC control-to-output for the linearized models.

Difference Structure DC/DC	Initial Value Status (S,T)/(W/m ² , °C)	Perturbation Value Status (S,T)/(W/m ² , °C)	$C(S,T)$	$d(S,T)$	$t_d/(s)$	$t_p/(s)$	$t_r/(s)$	$t_s/(s)$
Buck	400,10	1000,40	73.26	0.297	0.207	0.836	0.414	0.537
	800,30	1000,40	70.72	0.070	0.100	0.449	0.200	0.273
	1000,40	800,10	68.52	0.104	0.071	0.194	0.142	0.159
Boost	400,10	1000,40	73.26	0.306	0.181	0.393	0.361	1.083
	800,30	1000,40	70.72	0.053	0.078	0.224	0.156	1.433
	1000,40	800,10	68.52	0.074	0.081	0.246	0.162	1.614
Buck-Boost	400,10	1000,40	73.26	0.122	0.112	0.298	0.224	1.311
	800,30	1000,40	70.72	0.024	0.107	0.326	0.214	1.621
	1000,40	800,10	68.52	0.033	0.113	0.344	0.225	1.544

In addition, the linearized model dynamic performance index values in Figures 7–12 are approximately equal to the dynamic performance index values computed in Tables 4 and 5. The above findings further verify that the linearized model of the DC side has good practicality and feasibility.

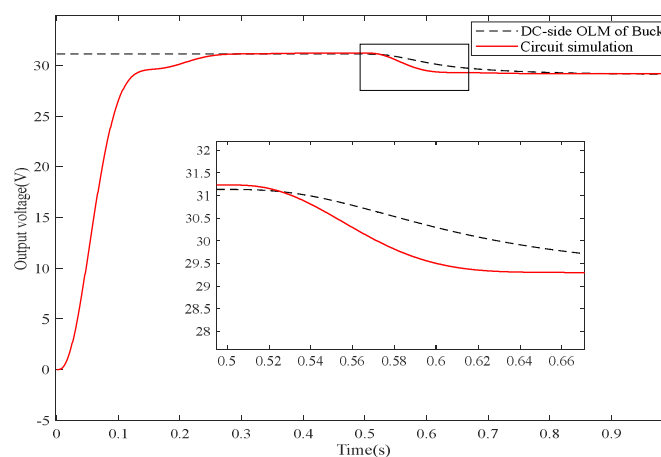


Figure 7. Response plots of the PV-Buck circuit structure input-to-output.

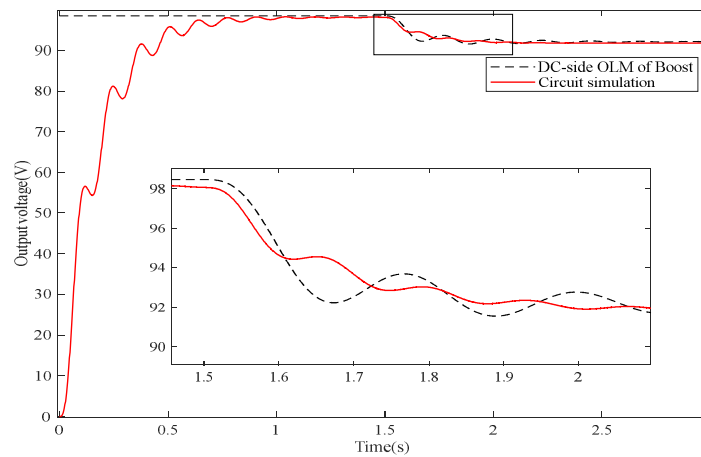


Figure 8. Response plots of the PV-Boost circuit structure input-to-output.

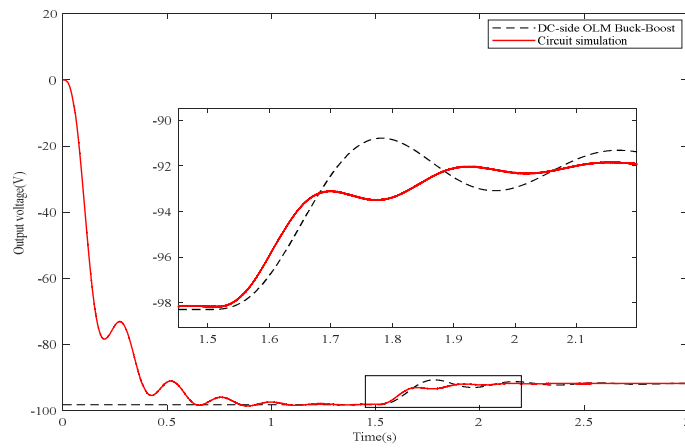


Figure 9. Response plot of the PV-Buck-Boost circuit structure input-to-output.

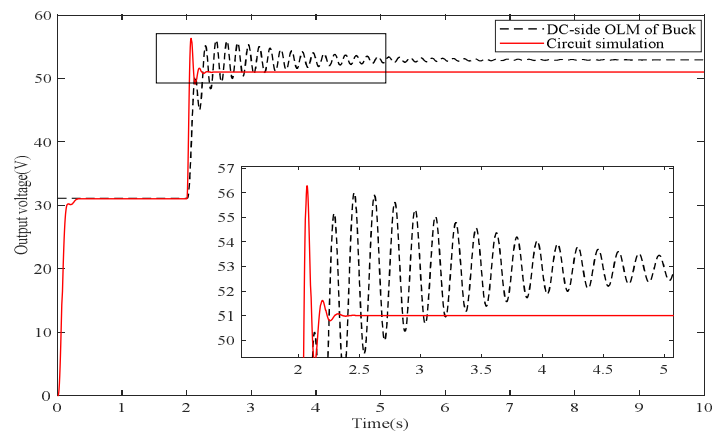


Figure 10. Response plot of the PV-Buck circuit structure control-to-output.

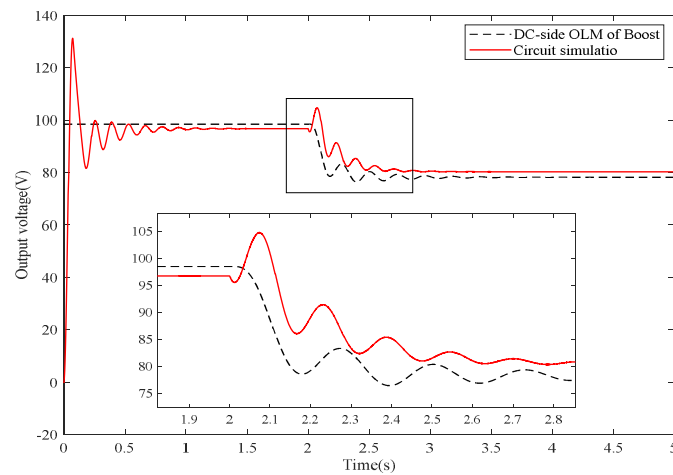


Figure 11. Response plot of the PV-Boost circuit structure control-to-output.

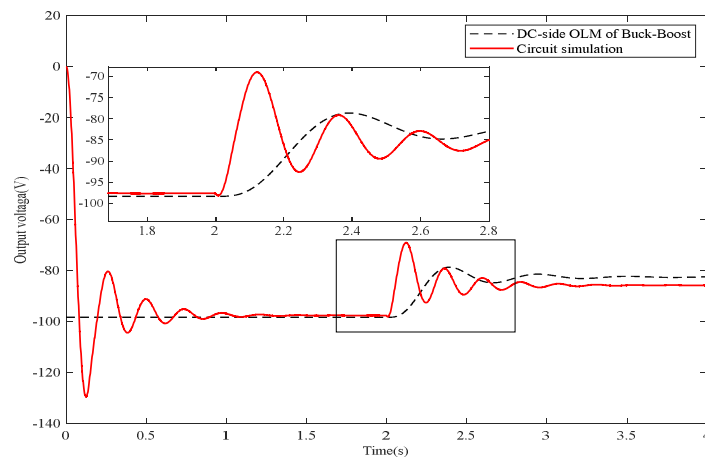


Figure 12. Response plot of the PV-Buck-Boost circuit structure control-to-output.

3.1.2. SOLM-VWP Verification of the PV System

The OLM-VWP of the PV system with the VWP is given by Equations (29)–(34). To completely eliminate the complexity of modeling a PV system and to improve the utility and convenience of the associated linearized models, based on the Routh approximation SOLM-VWP is proposed. Equations (35)–(42) to the second-order model Equation (43) by reducing the order of the sixth-order transfer function model, which can still retain low- and medium-frequency characteristics.

Then, simulation comparison experiments between the higher-order model and the reduced-order (second-order) model are conducted using MATLAB software to verify the model's accuracy. In these experiments, Equations (35)–(43) are verified under the condition that the PV system is subjected to small perturbation signals of irradiance and temperature as step signals. The results of these experiments are shown in Figures 13–18. These dynamic characteristics of the linearized model can be analyzed via the figures. In the case where the weather variables and control variables are the inputs, these analyzed linearized models include the PV system with the PV-Buck circuit, PV-Boost circuit, and PV-Buck-Boost circuit structures. Figures 13 and 16 show that the dynamic performance of the higher-order system and the second-order system with the PV-Buck circuit structure is basically the same. This result indicates that the second-order model established using Equation (43) can successfully analyze the dynamic performance of the higher-order system. Figures 14, 15, 17 and 18 show that the dynamic performance of the PV-Boost circuit and PV-Buck-Boost circuit high-order systems and second-order systems are basically the same. Although some errors remain, they are within the allowed range of the system, indicating

that the dynamic performance of the high-order system can also be effectively analyzed using the reduced-order model.

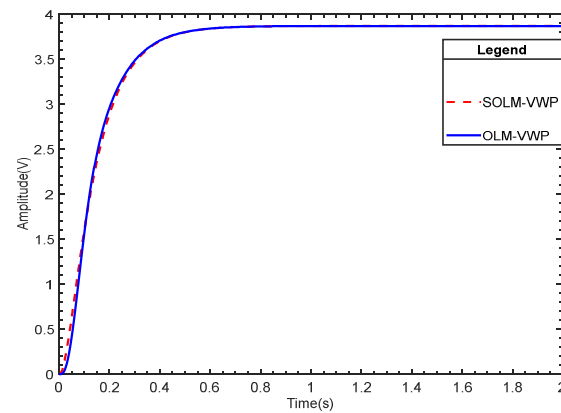


Figure 13. Comparison of PV-Buck circuit OLM-VWP and SOLM-VWP response for input condition.

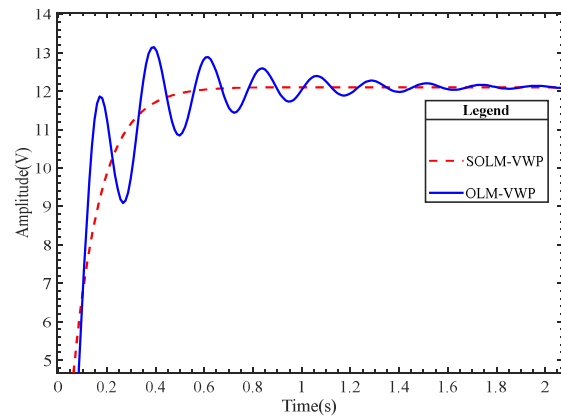


Figure 14. Comparison of PV-Boost circuit OLM-VWP and SOLM-VWP response for input condition.

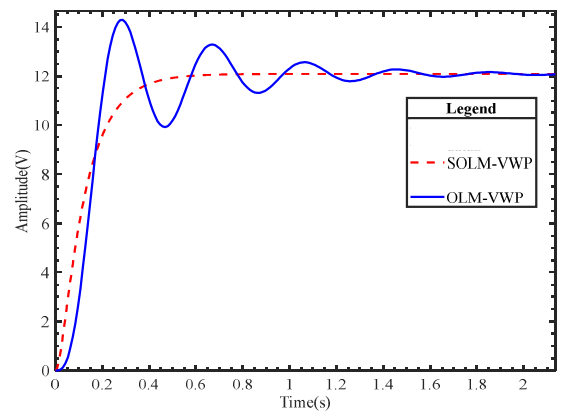


Figure 15. Comparison of PV-Buck-Boost circuit OLM-VWP and SOLM-VWP response for input condition.

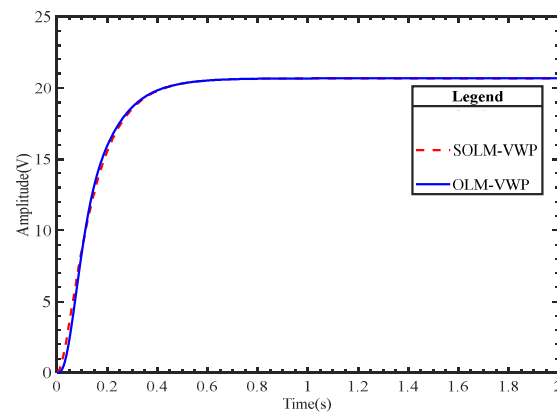


Figure 16. Comparison of PV-Buck circuit OLM-VWP and SOLM-VWP response for control condition.

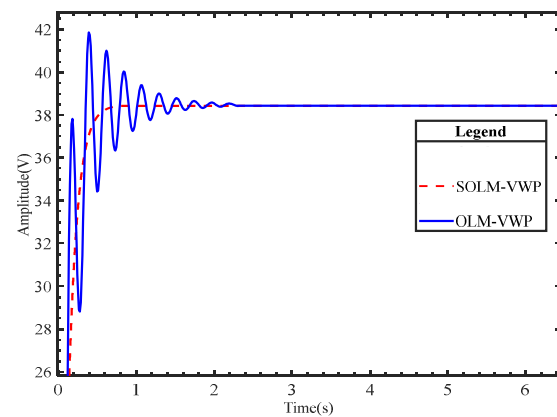


Figure 17. Comparison of PV-Boost circuit OLM-VWP and SOLM-VWP response for control condition.

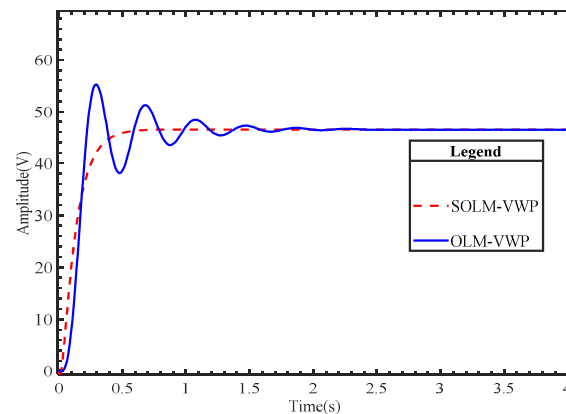


Figure 18. Comparison of PV-Buck-Boost circuit OLM-VWP and SOLM-VWP response for control condition.

3.1.3. Linearized Modeling of the PV System for Verification

To verify the OLM-VWP of the PV system and its simplified model proposed in Section 2.3, the following simulation experiments are conducted to analyze the feasibility and usability of the model. The experiments are carried out by building the PV system circuit model in MATLAB/Simulink, as well as the linearized mathematical model of the system, to simulate the dynamic response characteristics. The simulation experiments are carried out in two aspects. On the one hand, the simulation is intended to verify the OLM-VWP of the PV system from the small input perturbation to the output. On the other hand, the dynamic response characteristics of the model are verified by simulating the OLM-VWP of the PV system from a small control disturbance to the output. In this case,

the SOLM-VWP is represented by a second-order model in the simulation experiment. The simulation experiment is based on the circuit structure of the PV system in Figure 2, in which the DC/DC is chosen as a Buck circuit, Boost circuit, or Buck–Boost circuit structure, and the DC/AC is chosen as a full-bridge inverter circuit. These constitute the PV-Buck circuit, PV-Boost circuit, and PV-Buck–Boost circuit structures of the PV system.

To better analyze the dynamic characteristics of the OLM-VWP, the simulated circuit is verified under the situation in which the S and T steady-state values are $400 \text{ W/m}^2, 10 \text{ }^\circ\text{C}$ and the perturbation is $1000 \text{ W/m}^2, 25 \text{ }^\circ\text{C}$. The OLM-VWP of the PV system is verified using a simulation with ideal and nonideal circuit components. In the nonideal case, the parameters of the simulated circuit are as given in Table 3. For the experimental conditions in Section 3.1.1, three classic data sets are chosen to characterize the operation of the system over one day. In addition, the small perturbations are experimentally verified for three cases: varying S with constant T , constant S with varying T , and varying S with varying T .

(1) Validation of the OLM-VWP from input-to-output

Figures 19 and 20 show the case of a perturbation signal that has been fed to the simulation at 0.5 s; the simulated circuit and the linearized mathematical model in both figures stabilize after 0.98 s. Moreover, the experimental results of the circuit simulation and the OLM-VWP for the small signal are approximately equal in the ideal and nonideal cases. Figure 19 indicates that the linearized model of the PV system can be stable at the steady-state point of 1.02 s.

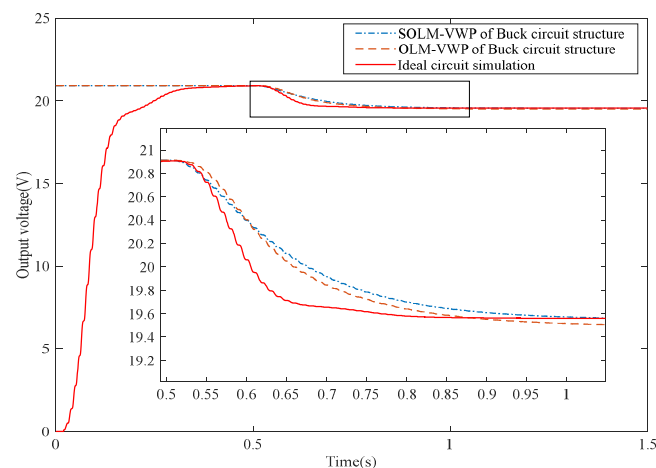


Figure 19. Simulation diagram of the PV-Buck system under ideal conditions.

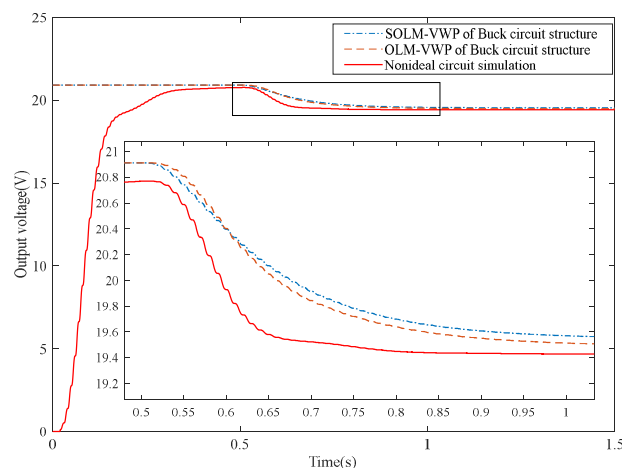


Figure 20. Simulation diagram of the PV-Buck system under nonideal conditions.

The circuit simulation already reaches the steady-state point at only 0.87 s, and the error in reaching the steady-state point is approximately 2%. Simulation experiments are performed to analyze the accuracy of OLM-VWP and SOLM-VWP, and the results are shown in Table 6, where $c(S, T)$, $D_{\max}(S, T)$, t_d , t_p , t_r , and t_s can be calculated using Equations (28) and (29) and Table 1 to evaluate the dynamic performance index of the PV-Buck circuit structure.

Table 6. Simulation results of the PV-Buck system with different inputs $c(S, T)$.

Initial Value Status (S,T)/(W/m ² , °C)	Perturbation Value Status (S,T)/(W/m ² , °C)	$c(S,T)$	$D_{\max}(S,T)$	t_d (s)	t_p (s)	t_r (s)	t_s (s)
1000,25	800,25	1.95	0.702	0.077	0.3582	0.14	0.155
800,25	600,25	0.35	0.633	0.142	0.4405	0.239	0.283
600,25	400,25	1.02	0.539	0.153	0.416	0.282	0.305
1000,10	1000,40	6.14	0.684	0.105	0.305	0.166	0.209
800,10	600,40	6.15	0.618	0.141	0.462	0.224	0.281
400,10	400,40	6.09	0.425	0.293	0.836	0.500	0.597
400,10	1000,40	4.74	0.425	0.265	0.836	0.447	0.529
800,20	1000,25	0.78	0.627	0.134	0.449	0.209	0.279
1000,40	800,10	4.19	0.722	0.076	0.193	0.14	0.152

The dynamic characteristic indexes calculated in Table 6 are exactly consistent with the simulation results in Figure 19, but the rise and delay times still have an error of approximately 2%. These results reveal the feasibility, usability, and rationality of the OLM-VWP and SOLM-VWP for different $c(S, T)$ conditions.

Figures 21 and 22 show a case in which a perturbation signal has been fed to the simulation experiment at 1 s; the simulated circuit and the linearized mathematical model in both figures stabilize after 2.14 s. Moreover, the experimental results of the circuit simulation and the OLM-VWP for the small signal are approximately equal in the ideal and nonideal cases. Figure 21 indicates that the linearized model of the PV system can be stable at the steady-state point of 2.07 s.

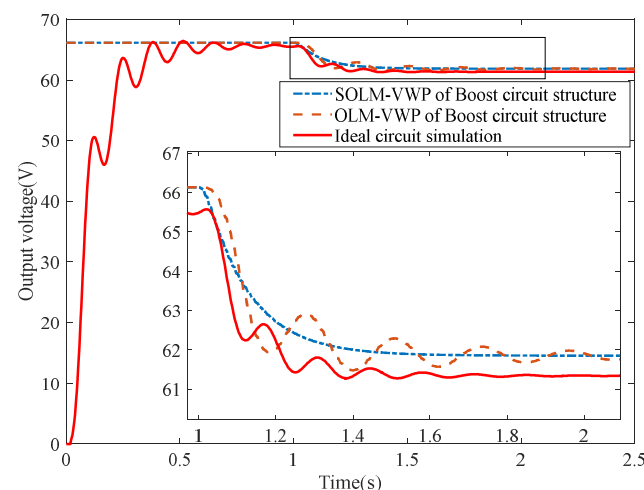


Figure 21. Simulation diagram of the PV-Boost system under ideal conditions.

The circuit simulation already reaches the steady-state point at only 1.81 s, and the error in reaching the steady-state point is approximately 4%. Simulation experiments are performed to analyze the accuracy of OLM-VWP and SOLM-VWP, and the results are shown in Table 7, where $c(S, T)$, $D_{\max}(S, T)$, t_d , t_p , t_r , and t_s can be calculated using Equations (28) and (30) and Table 1 to evaluate the dynamic performance index of the PV-Boost circuit structure. The dynamic characteristic indexes calculated in Table 7 are exactly consistent with the simulation results in Figure 21, but the rise time and delay time

still have an error of approximately 1%. These results reveal the feasibility, usability, and rationality of the OLM-VWP and SOLM-VWP for different $c(S, T)$ conditions.

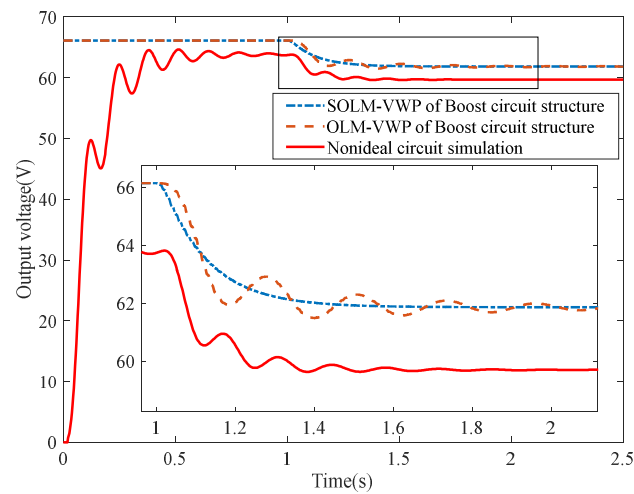


Figure 22. Simulation diagram of the PV-Boost system under nonideal conditions.

Table 7. Simulation results of the PV-Boost system with different inputs $c(S, T)$.

Initial Value Status $(S, T)/(W/m^2, ^\circ C)$	Perturbation Value Status $(S, T)/(W/m^2, ^\circ C)$	$c(S, T)$	$D_{max}(S, T)$	$t_d/(s)$	$t_p/(s)$	$t_r/(s)$	$t_s/(s)$
1000,25	800,25	1.95	0.549	0.073	0.226	0.144	1.557
800,25	600,25	0.35	0.500	0.071	0.215	0.143	1.429
600,25	400,25	1.02	0.414	0.070	0.198	0.449	1.357
1000,10	1000,40	6.14	0.537	0.071	0.222	0.144	1.525
800,10	600,40	6.15	0.488	0.070	0.211	0.141	1.398
400,10	400,40	6.094	0.256	0.175	0.293	0.351	1.072
400,10	1000,40	4.74	0.256	0.174	0.393	0.351	1.072
800,20	1000,25	0.78	0.496	0.069	0.214	0.141	1.418
1000,40	800,10	4.19	0.562	0.073	0.232	0.147	1.586

Figures 23 and 24 show the case in which a perturbation signal has been fed to the simulation experiment at 1.5 s; the simulated circuit and the linearized mathematical model in both figures stabilize after 3.12 s. Moreover, the experimental results of the circuit simulation and the OLM-VWP for the small signal are approximately equal in the ideal and nonideal cases. Figure 23 indicates that the linearized model of the PV system can be stable at the steady-state point of 3.03 s. The circuit simulation already reaches the steady-state point at only 2.48 s, and the error in reaching the steady-state point is approximately 2%.

Simulation experiments are performed to analyze the accuracy of OLM-VWP and SOLM-VWP, and the results are shown in Table 8 where $c(S, T)$, $D_{max}(S, T)$, t_d , t_p , t_r , and t_s can be calculated using Equations (28) and (31) and Table 1 to evaluate the dynamic performance index of the PV-Buck–Boost circuit structure. The dynamic characteristic indexes calculated in Table 8 are exactly consistent with the simulation results in Figure 23, but the rise time and delay time still have an error of approximately 3%. These results reveal the feasibility, usability, and rationality of the OLM-VWP and SOLM-VWP for different $c(S, T)$ conditions.

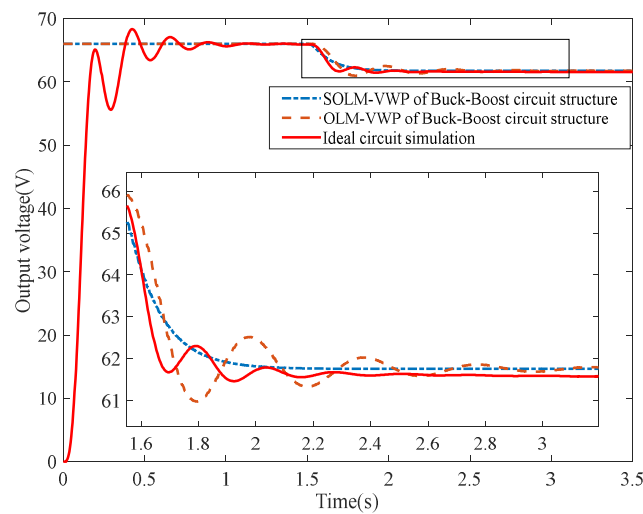


Figure 23. Simulation diagram of the PV-Buck-Boost system under ideal conditions.

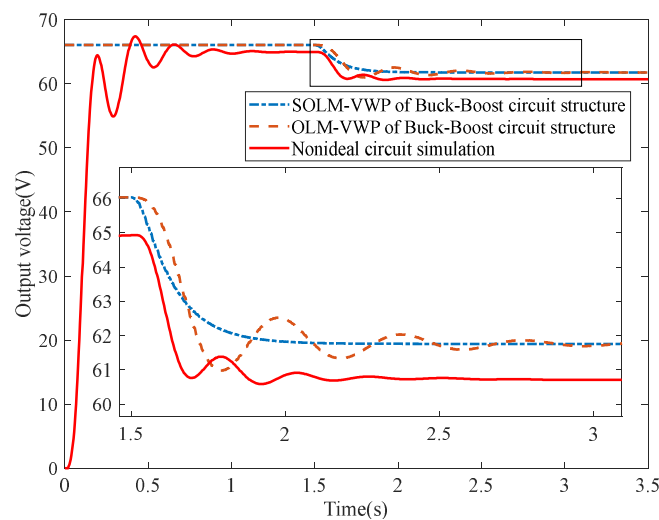


Figure 24. Simulation diagram of the PV-Buck-Boost system under nonideal conditions.

Table 8. Simulation results of the PV-Buck-Boost system with different inputs $c(S, T)$.

Initial Value Status (S, T)/($W/m^2, ^\circ C$)	Perturbation Value Status (S, T)/($W/m^2, ^\circ C$)	$c(S, T)$	$D_{max}(S, T)$	$t_d/(s)$	$t_p/(s)$	$t_r/(s)$	$t_s/(s)$
1000,25	800,25	1.95	0.689	0.118	0.388	0.249	1.515
800,25	600,25	0.35	0.666	0.115	0.383	0.249	1.515
600,25	400,25	1.02	0.630	0.119	0.383	0.246	1.516
1000,10	1000,40	6.14	0.683	0.119	0.383	0.249	1.514
800,10	600,40	6.15	0.661	0.117	0.383	0.247	1.515
400,10	400,40	6.09	0.573	0.123	0.386	0.248	1.536
400,10	1000,40	4.74	0.573	0.112	0.386	0.224	1.536
800,20	1000,25	0.78	0.665	0.118	0.383	0.249	1.516
1000,40	800,10	4.19	0.695	0.117	0.383	0.230	1.516

(2) Validation of the OLM-VWP from Control-to-Output

As above, Figures 25 and 26 show that a perturbation signal is fed to the simulation experiment at 2 s, and the simulated circuit and the linearized mathematical model in both figures stabilize after 2.53 s. Moreover, the experimental results of the circuit simulation and the OLM-VWP for the small signal are approximately equal in ideal and nonideal cases. Additionally, from the analysis in Figure 25, it can be concluded that the linearized model of

the PV system can be stable at the steady-state point of 2.53 s. The circuit simulation already reaches the steady-state point at only 2.47 s, and the error in reaching the steady-state point is approximately 4%.

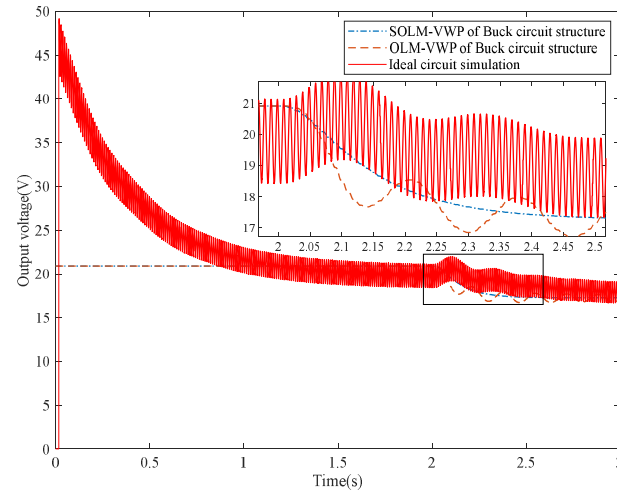


Figure 25. Simulation diagram of the PV-Buck system under ideal conditions.

On the other hand, some simulation experiments were performed to analyze the accuracy of OLM-VWP and SOLM-VWP, and the results are shown in Table 9 where $C(S, T)$, $d(S, T)$, t_d , t_p , t_r , and t_s can be calculated using Equations (28) and (32) and Table 1 to evaluate the dynamic performance index of the PV-Buck circuit structure. Among them, the dynamic characteristic indexes calculated in Table 9 are exactly consistent with the simulation results in Figure 25, but the rise time and delay time still have an error of approximately 5%. Clearly, these results reveal the feasibility, usability, and rationality of the OLM-VWP and SOLM-VWP for different $d(S, T)$ conditions.

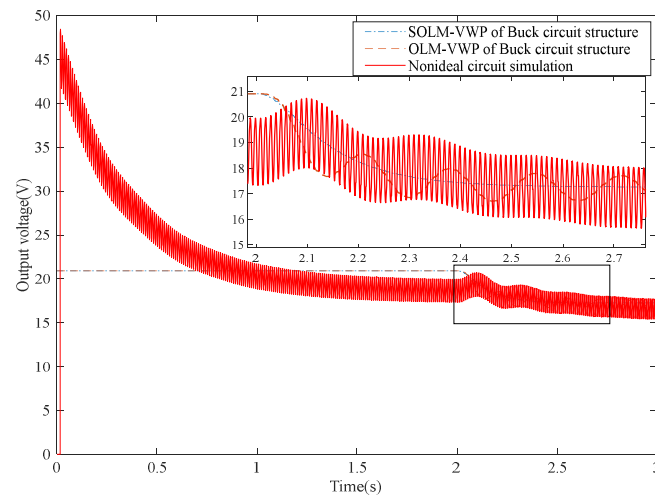


Figure 26. Simulation diagram of the PV-Buck system under nonideal conditions.

As above, Figures 27 and 28 show that a perturbation signal is fed to the simulation experiment at 1 s, and the simulated circuit and the linearized mathematical model in both figures stabilize after 2.1 s. Moreover, the experimental results of the circuit simulation and the OLM-VWP for the small signal are approximately equal in the ideal and nonideal cases. Additionally, from the analysis in Figure 27, it can be concluded that the linearized model of the PV system can be stable at the steady-state point of 2.08 s. However, the circuit simulation already reaches the steady-state point at only 1.88 s, and the error in reaching the steady-state point is approximately 3%.

Table 9. Simulation results of the PV-Buck system at different inputs $d(S, T)$.

Initial Value Status (S, T)/($W/m^2, ^\circ C$)	Perturbation Value Status (S, T)/($W/m^2, ^\circ C$)	$C(S, T)$	$d(S, T)$	t_d (s)	t_p (s)	t_r (s)	t_s (s)
1000,25	800,25	71.50	0.049	0.079	0.242	0.160	1.576
800,25	600,25	69.55	0.086	0.076	0.225	0.154	1.444
600,25	400,25	69.20	0.157	0.075	0.204	0.152	1.370
1000,10	1000,40	74.66	0.025	0.081	0.239	0.160	1.546
800,10	600,40	72.71	0.065	0.076	0.221	0.155	1.413
400,10	400,40	73.26	0.001	0.176	0.393	0.361	1.083
400,10	1000,40	73.26	0.306	0.175	0.393	0.361	1.083
800,20	1000,25	70.72	0.053	0.076	0.224	0.156	1.433
1000,40	800,10	68.52	0.074	0.081	0.246	0.162	1.614

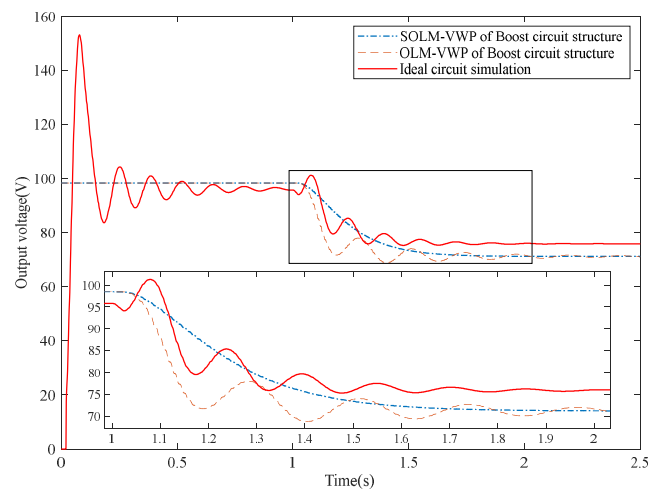


Figure 27. Simulation diagram of the PV-Boost system under ideal conditions.

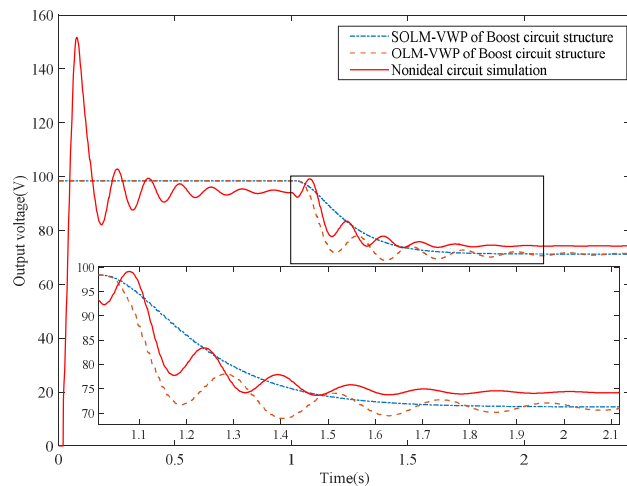


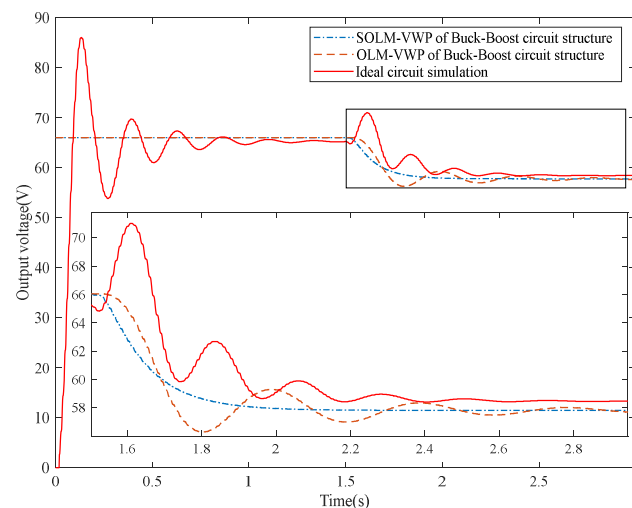
Figure 28. Simulation diagram of the PV-Boost system under nonideal conditions.

On the other hand, some simulation experiments were performed to analyze the accuracy of OLM-VWP and SOLM-VWP, and the results are shown in Table 10 where $C(S, T)$, $d(S, T)$, t_d , t_p , t_r , and t_s can be calculated using Equations (28) and (33) and Table 1 to evaluate the dynamic performance index of the PV-Boost circuit structure. Among them, the dynamic characteristic indexes calculated in Table 10 are exactly consistent with the simulation results in Figure 27, but the rise time and delay time still have an error of approximately 2%. Clearly, these results reveal the feasibility, usability, and rationality of the OLM-VWP and SOLM-VWP for different $d(S, T)$ conditions.

Table 10. Simulation results of the PV-Boost system at different inputs $d(S, T)$.

Initial Value Status (S, T)/($W/m^2, ^\circ C$)	Perturbation Value Status (S, T)/($W/m^2, ^\circ C$)	$C(S, T)$	$d(S, T)$	t_d (s)	t_p (s)	t_r (s)	t_s (s)
1000,25	800,25	71.50	0.049	0.079	0.242	0.160	1.576
800,25	600,25	69.55	0.086	0.076	0.225	0.154	1.444
600,25	400,25	69.20	0.157	0.075	0.204	0.152	1.370
1000,10	1000,40	74.66	0.025	0.081	0.239	0.160	1.546
800,10	600,40	72.71	0.065	0.076	0.221	0.155	1.413
400,10	400,40	73.26	0.001	0.176	0.393	0.361	1.083
400,10	1000,40	73.26	0.306	0.175	0.393	0.361	1.083
800,20	1000,25	70.72	0.053	0.076	0.224	0.156	1.433
1000,40	800,10	68.52	0.074	0.081	0.246	0.162	1.614

Figures 29 and 30 show the case of a perturbation signal fed to the simulation experiment at 1.5 s; the simulated circuit and the linearized mathematical model in both figures stabilize after 2.86 s. Moreover, the experimental results of the circuit simulation and the OLM-VWP for the small signal are approximately equal in the ideal and nonideal cases. Figure 29 indicates that the linearized model of the PV system can be stable at the steady-state point of 2.81 s. The circuit simulation already reaches the steady-state point at only 2.67 s, and the error in reaching the steady-state point is approximately 2%. Simulation experiments are performed to analyze the accuracy of OLM-VWP and SOLM-VWP, and the results are shown in Table 11 where $C(S, T)$, $d(S, T)$, t_d , t_p , t_r , and t_s can be calculated using Equations (28) and (34) and Table 1 to evaluate the dynamic performance index of the PV-Buck–Boost circuit structure. The dynamic characteristic indexes calculated in Table 11 are exactly consistent with the simulation results in Figure 29, but the rise time and delay time still have an error of approximately 2%. These results reveal the feasibility, usability, and rationality of the OLM-VWP and SOLM-VWP for different $d(S, T)$ conditions.

**Figure 29.** Simulation diagram of the PV-Buck–Boost system under ideal conditions.

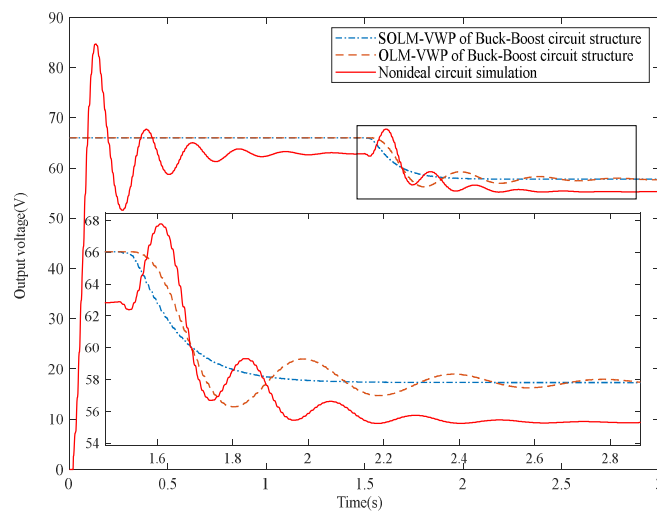


Figure 30. Simulation diagram of the PV-Buck-Boost system under nonideal conditions.

Table 11. Simulation results of the PV-Buck-Boost system at different inputs $d(S, T)$.

Initial Value Status (S, T)/($W/m^2, ^\circ C$)	Perturbation Value Status (S, T)/($W/m^2, ^\circ C$)	$C(S, T)$	$d(S, T)$	t_d /(s)	t_p /(s)	t_r /(s)	t_s /(s)
1000,25	800,25	71.50	0.023	0.111	0.340	0.223	1.520
800,25	600,25	69.55	0.036	0.106	0.326	0.219	1.621
600,25	400,25	69.20	0.056	0.106	0.305	0.217	1.487
1000,10	1000,40	74.66	0.012	0.111	0.335	0.219	1.496
800,10	600,40	72.71	0.02	0.107	0.321	0.215	1.609
400,10	400,40	73.26	0.001	0.111	0.298	0.223	1.310
400,10	1000,40	73.26	0.122	0.114	0.298	0.223	1.310
800,20	1000,25	70.72	0.024	0.111	0.326	0.219	1.621
1000,40	800,10	68.52	0.033	0.115	0.343	0.225	1.545

3.1.4. Theoretical Verification of Small-Signal Delay in the PV System

The proposed DTM-VWP for the PV system is validated by using the validation method in Figure 31. MATLAB simulation software is used to analyze and compare the time delay of SOLM-VWP and DTM-VWP. In Figures 32–37, the solid line shows the simulation data of the OLM-VWP, and the dashed line represents the DTM-VWP derived from the curve fitting. Three circuits, the Buck circuit, Boost circuit, and Buck-Boost circuit, are simulated under the conditions of small-disturbance signals with inputs $c(S, T)$ and $d(S, T)$.

$$t(v_t) = \frac{-134.6v_t^2 - 31.12v_t + 2161}{v_t^3 + 3006v_t^2 - 2.554 \times 10^4 v_t + 5.38 \times 10^4} \tag{51}$$

$$t(v_t) = \frac{-0.7795 v_t^2 + 9.597v_t - 1.558}{v_t^3 - 24.28v_t^2 + 129.7 v_t + 214.4} \tag{52}$$

$$t(v_t) = \frac{3.707v_t^3 - 95.08 v_t^2 + 607.9v_t - 2.958}{v_t^5 - 45.41v_t^4 + 795.8v_t^3 - 6409v_t^2 + 2.004 \times 10^4 v_t - 95.25} \tag{53}$$

Similarly, the DTM-VWP of the PV-Buck circuit, PV-Boost circuit, and PV-Buck-Boost circuit structure systems can be represented by Equations (54)–(56) under the condition of a small perturbation signal of the input $d(S, T)$ to the output v_o , as shown in Figures 35–37.

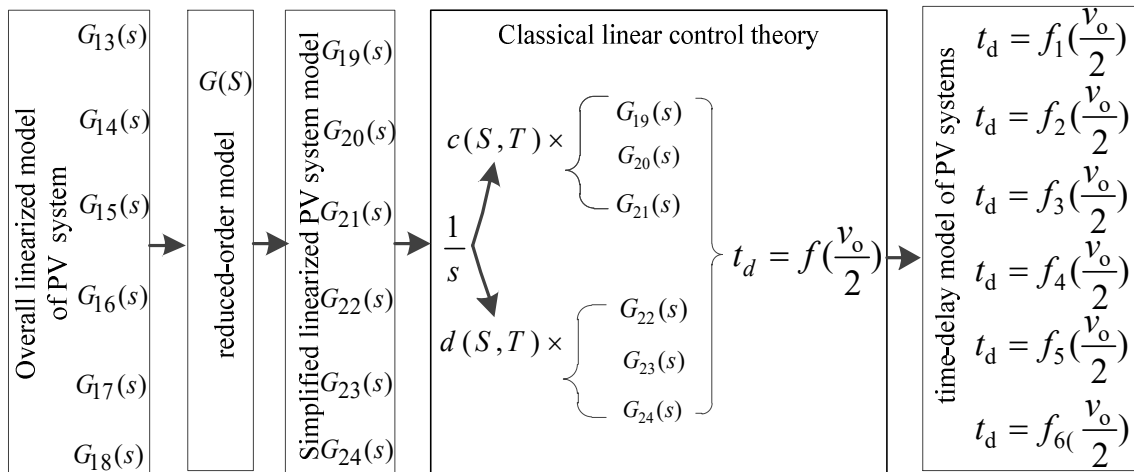


Figure 31. Validation method of the DTM-VWP for the PV system.

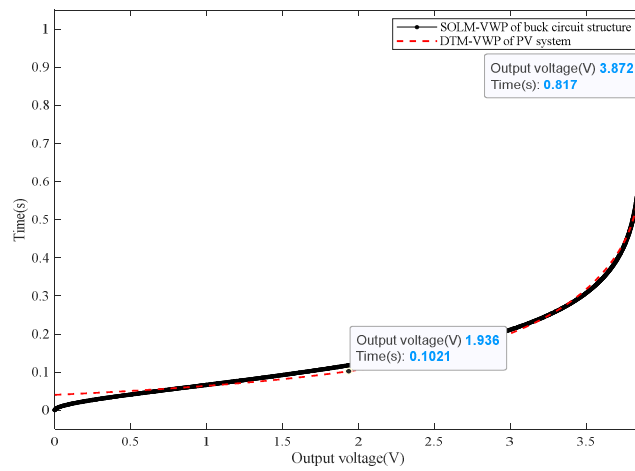


Figure 32. Comparison of SLOM-VWP and DTM-VWP delay times for PV-Buck systems under inputted disturbance conditions.

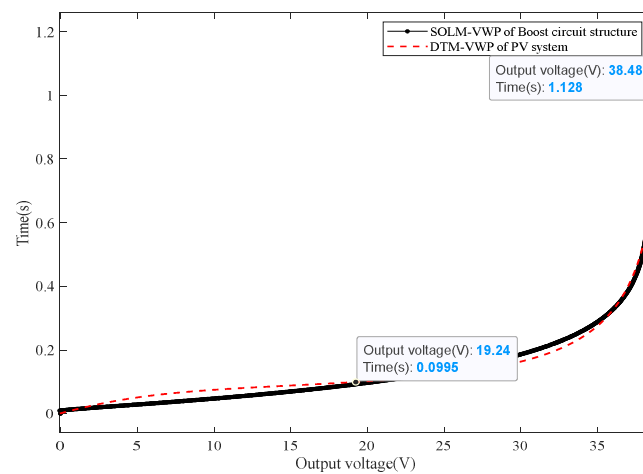


Figure 33. Comparison of SLOM-VWP and DTM-VWP delay times for PV-Boost systems under inputted disturbance conditions.

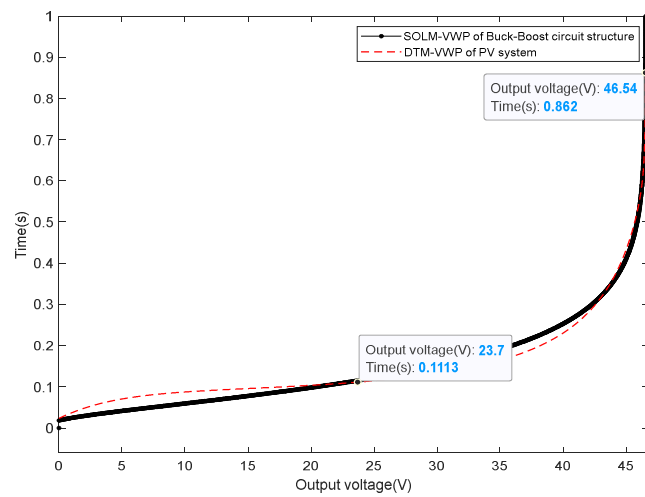


Figure 34. Comparison of SLOM-VWP and DTM-VWP delay times for PV-Buck–Boost systems under inputted disturbance conditions.

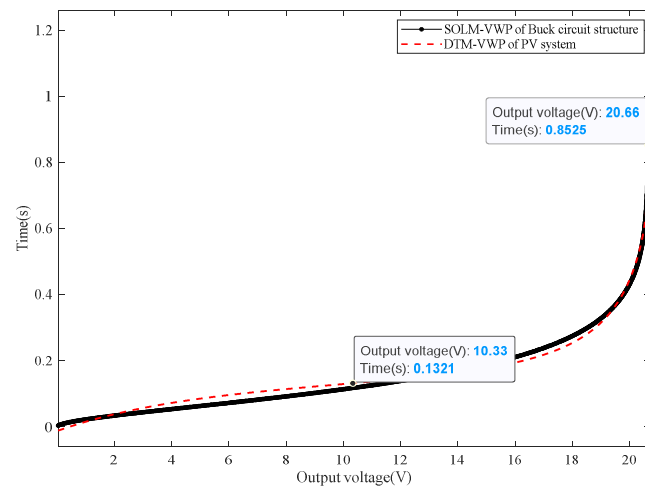


Figure 35. Comparison of SLOM-VWP and DTM-VWP delay times for PV-Buck systems under controlled disturbance conditions.

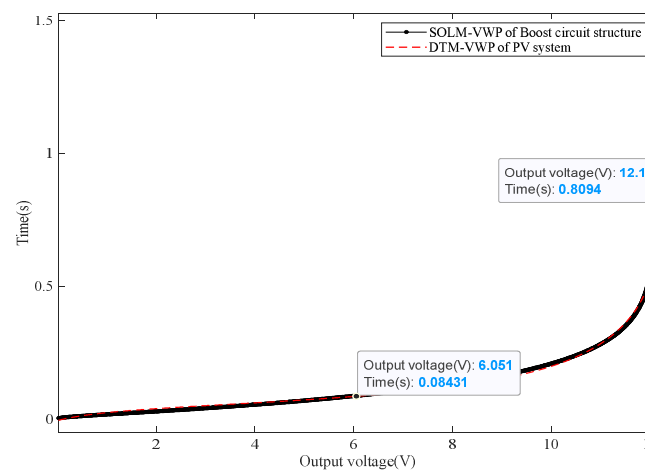


Figure 36. Comparison of SLOM-VWP and DTM-VWP delay times for PV-Boost systems under controlled disturbance conditions.

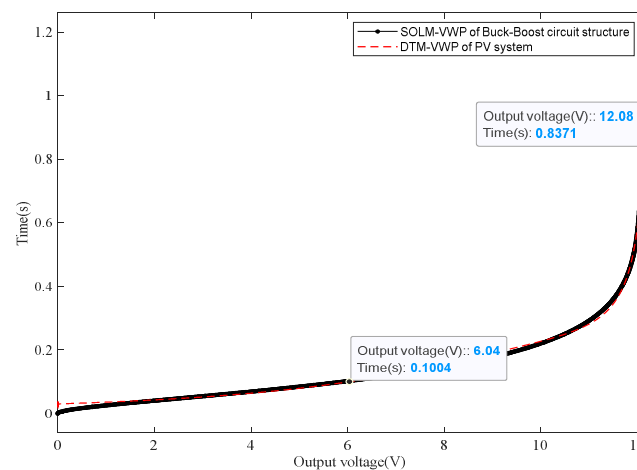


Figure 37. Comparison of SLOM-VWP and DTM-VWP delay times for PV-Buck–Boost systems under controlled disturbance conditions.

$$t(v_t) = \frac{3.399v_t^3 - 179.8v_t^2 + 2311v_t - 932.8}{v_t^4 - 23.09v_t^3 - 208.7v_t^2 + 1689v_t + 7.562 \times 10^4} \tag{54}$$

$$t(v_t) = \frac{-0.33v_t^4 - 52.04v_t^3 + 2452v_t^2 + 1624v_t + 128.8}{v_t^5 - 71.87v_t^4 + 1094v_t^3 + 2207v_t^2 + 1.952 \times 10^5v_t + 1.091 \times 10^5} \tag{55}$$

$$t(v_t) = \frac{-0.6571v_t^4 - 68.01v_t^3 + 4395v_t^2 + 9326v_t + 4179}{v_t^5 - 84.09v_t^4 + 1240v_t^3 + 1.737 \times 10^4v_t^2 + 2.873 \times 10^5v_t + 1.792 \times 10^5} \tag{56}$$

The above equations show that the delay time of the system can be calculated using Equations (51)–(56) for small disturbances of the PV system. In addition, the simulation results of DTM-VWP and SOLM-VWP have small errors, and the error analysis of the DTM-VWP results is shown in Table 12. This result is acceptable for engineering applications. Therefore, it can be concluded that DTM-VWP is very accurate under different $c(S, T)$ and $d(S, T)$ conditions.

Table 12. DTM-VWP error result analysis.

Different Conditions of Input	Different Circuit Structures	SEE	RMSR (%)
Inputted disturbance	Buck	1.598	1.264%
	Boost	0.969	0.984%
	Buck–Boost	1.716	1.196%
Controlled disturbance	Buck	3.071	1.615%
	Boost	4.065	1.842%
	Buck–Boost	5.029	2.041%

3.2. Experimental Validation

To validate the linearized modeling method and DTM-VWP, the PV system shown in Figure 2 is simulated in Simulink software and prototyped for physical verification in the laboratory. The experimental platform for the PV-Buck and the PV-Boost systems is illustrated in Figure 38. The circuit parameters used for the experiments are given in Table 12, where the DC/DC is selected as the bidirectional DC/DC circuit for the experiments, the DC/AC is used as the full-bridge inverter, the STM32 is selected as the digital controller, and the load is a purely resistive load. These components can be used to verify both PV-Buck circuit structure and PV-Boost structure systems.

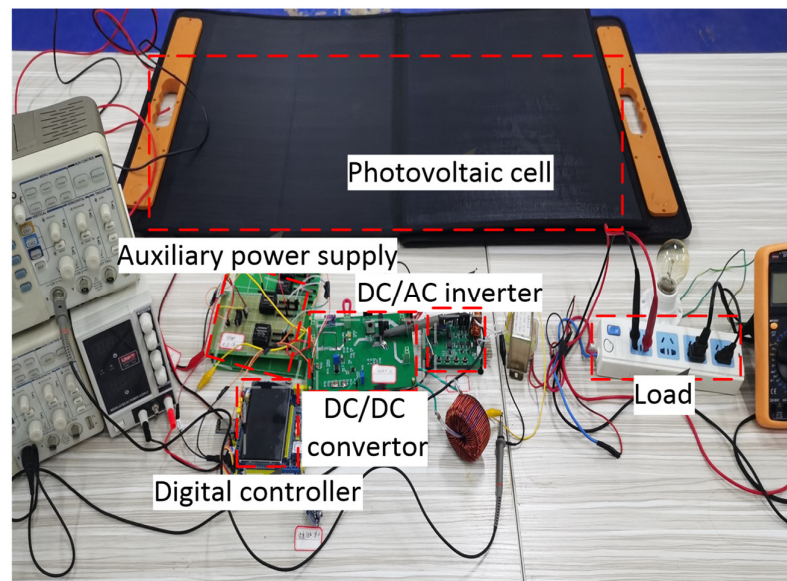


Figure 38. The PV system physical verification circuit.

Figures 39 and 40 show the experimental plots of the DC-side linearization model of the PV-Buck system. Figure 39 is the experimental waveform with sudden irradiance change and constant temperature (400,25 to 1000,25). Figure 40 shows the experimental waveform for both irradiance and temperature changes (600,10 to 1000,45). Figures 41 and 42 show the experimental plots of the DC-side linearization model of the PV-Boost system. Figure 41 is the experimental waveform with sudden irradiance change and constant temperature (1000,25 to 400,25). Figure 42 shows the experimental waveform for both irradiance and temperature changes (800,20 to 1000,40). It can be seen from these figures that when the PV system reaches steady state and is suddenly disturbed by the input, it can be seen that the output voltage on the DC side will change, and there will be a certain delay time before reaching the next steady state. From Figure 39, it can be seen that the system DC-side output voltage reaches steady state at 0.43 V at 400,25, and when disturbed by 1000,25 the system DC-side output voltage changes by 0.26 V, generating a delay time of 12.82 ms before reaching the next steady state. Similarly, the analysis results of Figures 40–42 are similar to those of Figure 39, and the details are shown in Table 13, which indicates that the results are basically consistent with the previous theoretical simulation results. The validity of the DC-side linearization model of the PV system is further verified.



Figure 39. PV-Buck system with sudden irradiance disturbance.



Figure 40. PV-Buck system with sudden temperature and irradiance disturbances.

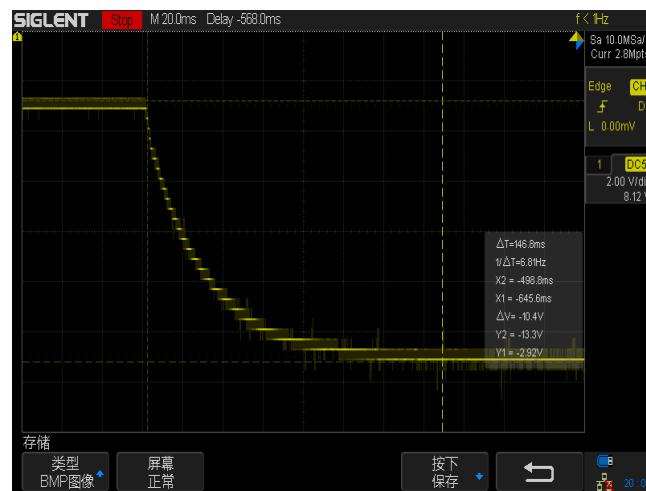


Figure 41. PV-Boost system with sudden irradiance disturbance.



Figure 42. PV-Boost system with sudden temperature and irradiance disturbances.

Table 13. Circuit parameters of the experiment.

PV-Buck Generation System Circuit Parameters								
Initial value status (S, T)/($W/m^2, ^\circ C$)	Perturbation value status (S, T)/($W/m^2, ^\circ C$)	Modulation ratio M	R_L	C_1	C_2	C_3	L_1	L_2
400,10	1000,40	0.95	5Ω	470 μF	1000 μF	1 μF	500 μH	3 mH
PV-Boost generation system circuit parameters								
Initial value status (S, T)/($W/m^2, ^\circ C$)	Perturbation value status (S, T)/($W/m^2, ^\circ C$)	Modulation ratio M	R_L	C_1	C_2	C_3	L_1	L_2
400,10	1000,40	0.95	53.3Ω	1000 μF	470 μF	1 μH	500 μF	3 mH

To validate the effectiveness of VWP-OLM for PV systems, the following physical experiments are conducted. Two common circuit structures (PV-Buck and PV-Boost) are selected for the experiments, respectively. The PV-Buck system is evaluated with an equivalent voltage of 51.2 V of the steady-state PV cell input. Figure 43 shows that the PV-Buck system operates at the MPP with a duty cycle D_M of 0.423. For input perturbation of the PV cell at a voltage of 34.7 V, the dynamic characteristics are shown in Figure 44. In addition, the dynamic response of the settling time and output voltage of its PV system can be analyzed from the figure.

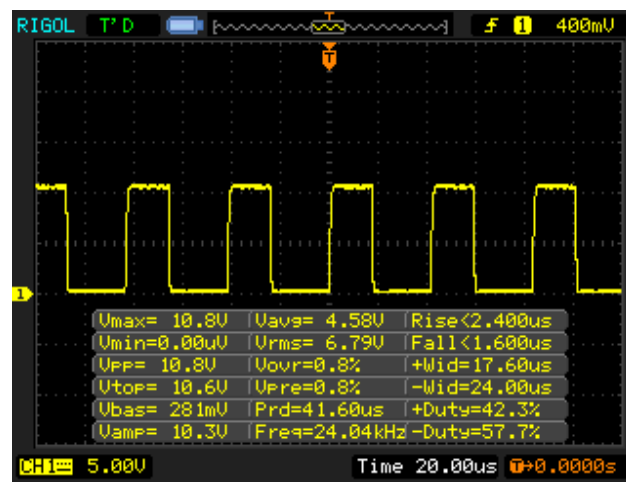


Figure 43. The duty cycle of the PV-Buck system at steady state.

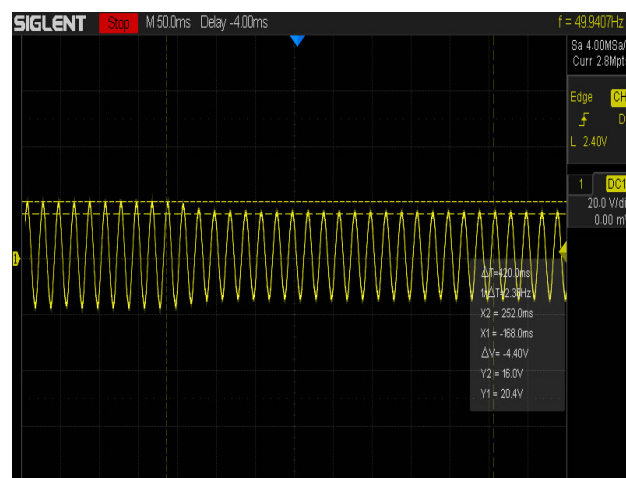


Figure 44. The output response of the PV-Buck system.

The PV-Boost system experiment is conducted with a PV cell equivalent input steady-state voltage of 13.13 V. From the analysis in Figure 45, the PV system operates at the

MPP when the duty cycle D_M is 0.256. When the input disturbance voltage is 18.32 V, the dynamic characteristics are as shown in Figure 46, which also shows the dynamic response of the settling time and the output voltage of the system. In summary, the results of this experiment are consistent with the simulation results in Section 3.1.3. However, there are still some errors in the results, as can be seen in the experimental results shown in Tables 14 and 15, which may be caused by the internal resistance of the diodes and switching tubes.

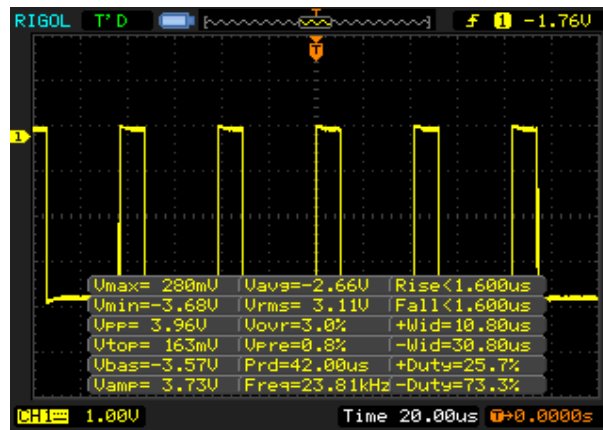


Figure 45. The duty cycle of the PV-Boost system at steady state.

Table 14. Experimental data to verify the linearization theory.

System Type	Initial Value Status (S,T)/($W/m^2, ^\circ C$)	Perturbation Value Status (S,T)/($W/m^2, ^\circ C$)	Output Voltage Variation	System Delay Time
PV-Buck	400,25	1000,25	2.60 V	12.82 ms
	600,10	100,45	0.384 V	12.5 ms
PV-Boost	1000,25	400,25	10 V	73 ms
	800,20	1000,40	1.57 V	21.75 ms

Table 15. Experimental data to verify the linearization theory corresponding to Figures 43–46.

System Type	Duty Cycle	Input Steady-State Voltage	Input Perturbation	Nonideal Condition Output Value	Ideal Condition Output Value	Nonideal Condition Output Value	Ideal Condition Output Value
PV-Buck	0.423	51.2 V	34.7 V	20.4 V	21.65 V	16.0 V	14.67 V
PV-Boost	0.256	13.13 V	18.32 V	16.4 V	17.64 V	23.2 V	24.62 V



Figure 46. The output response of the PV-Boost system.

4. Discussion

There are some errors in obtaining the equations using the curve fitting method. Equations (27), (28) and (51)–(56) provide the DTM-VWP. Therefore, one of the limitations of OLM-VWP and DTM-VWP is the presence of these errors, which are discussed as follows. First, Figures 19–30 indicate that the DTM-VWP and the simulated circuit always remain approximately the same in both the ideal case and the nonideal case regardless of S or T variations. Then, for the DTM-VWP, some errors exist. The analysis can be derived from Figures 32–37. As long as the circuit parameters are determined and the perturbations $c(S, T)$ and $d(S, T)$ are measurable, the system delay time can be calculated. The delay time error between the DTM-VWP and the SOLM-VWP is very small regardless of the perturbation variation. In practical applications, these errors can be ignored, making use of these OLMs suitably convenient. Finally, it is well known that almost all theoretical studies of simplified mathematical models inevitably lead to some errors. Therefore, these small errors in the theoretical analysis are acceptable.

In addition, all the SOLM-VWPs proposed are investigated on the basis of the OLM-VWP of the PV system with order reduction using the Routh approximation method. Therefore, the accuracy, reasonableness, and applicability of the delay time are constrained by the approximation method, which is another limitation of these models.

Although the OLM-VWP and SOLM-VWP have some drawbacks (or limitations), the combination of the MATLAB simulation analysis, the VWP methods, and the curve fitting techniques can still ensure the superiority and validity of these models. Methods to overcome these problems include error calibration and averaging methods.

5. Conclusions

The SOLM-VWP is given using the proposed small-signal linearized mathematical model. Based on this, the SOLM-VWP and the DTM-VWP of the system are proposed. Using the SOLM-VWP for analysis has the advantages of not only reducing the hardware cost, the computational burden, and the analysis complexity, but also of obtaining good transient and steady-state performance of the PV system. Finally, through simulation experiments, the accuracy and rationality of the proposed OLM-VWP of the PV system is illustrated. The feasibility and usability of the proposed OLM-VWP are verified regardless of irradiance and temperature variations, and the OLM-VWP is successfully implemented to calculate the transient performance indexes of the system. Moreover, the transient characteristics of the linearized model and the actual simulated circuit are basically equal when the simulation analysis is performed under ideal or nonideal conditions.

Planned future work on this topic focuses on the proposed DTM-VWP of the PV system for energy scheduling control methods, especially for real-time energy optimal scheduling methods. To achieve this, some existing improved power forecasts can be combined with the proposed DTM-VWP. Moreover, the real-time energy optimal scheduling method should be studied to eliminate the output power overshoot of the input grid.

Author Contributions: Conceptualization, S.L.; methodology, S.L. and X.Z.; software, X.Z.; validation, S.L., X.Z. and J.F.; formal analysis, X.Z.; investigation, S.L. and X.Z.; resources, X.Z.; data curation, X.Z.; writing—original draft preparation, X.Z.; writing—review and editing, S.L. and X.Z.; visualization, X.Z.; supervision, S.L.; project administration, S.L.; funding acquisition, S.L. All authors have read and agreed to the published version of the manuscript.

Funding: This work was supported by National Natural Science Foundation of China (No. 61963014).

Data Availability Statement: All relevant data are within the paper.

Acknowledgments: The authors would like to sincerely thank the editors and anonymous reviewers for their valuable comments and suggestions to improve the quality of the article.

Conflicts of Interest: The author declares no conflict of interest.

Abbreviations

PV	photovoltaic
MPP	maximum power point
MPPT	maximum power point tracking
PWM	pulse width modulation
VWP	variable weather parameters
AC	alternating current
DC	direct current
DC/AC	DC/AC inverter
OLM-VWP	overall linearized model with variable weather parameters
SOLM-VWP	simplified overall linearized model with variable weather parameters
DC/DC	DC/DC converter circuit
PLL	phase-locked loop
DTM-VWP	delay-time model with variable weather parameters

Nomenclature

$P_{\max}(S, T)$	power of the MPP	W
C_1	shunt capacitor of the PV cell	μF
C_2	filter capacitance of the DC/DC	μF
C_3	filter capacitance of the DC/AC	μF
L_1	power inductance of the DC/DC	μH
L_2	filter inductance of the DC/AC	mH
R_{eq}	equivalent series resistance of the PV cell	Ω
R_i	equivalent input resistance of the DC/DC	Ω
R_1	equivalent resistance at the output end of the DC/DC	Ω
R_L	equivalent resistance at the output end of the DC/AC	Ω
$C(S, T)$	weather parameters input	
$D_{\max}(S, T)$	duty ratio of the MPP	
r	internal resistance of filter capacitance of the DC/AC	Ω
D	modulation duty cycle of the DC/DC	
S	irradiance	W/m^2
T	temperature	$^{\circ}\text{C}$
V_m	reference sine wave signal of the modulator	V
V_{SM}	equivalent input voltage of the photovoltaic cell	V
V_{eq}	equivalent output voltage of the photovoltaic cell	V
I_{eq}	equivalent output current of the photovoltaic cell	A
V_d	DC/DC equivalent output voltage	V
I_d	DC/DC equivalent output current	A
V_o	DC/AC equivalent output voltage	V
I_o	DC/AC equivalent output current	V
t_d	delay time	s
t_r	rise time	s
t_s	settling time	s
t_p	peak time	s
d	small-disturbance input duty cycle of the controller of DC/DC	
v_d	output voltage of the small-signal input PV system	V
$c(S, T)$	small-disturbance input of the DC/DC	
$d(S, T)$	control input perturbation	
V_{tri}	the peak value of the triangular carrier wave	V
K_{pwm}	proportionality factor of the inverter control	
M	modulating ratio	

References

1. Hernández, J.C.; Bueno, P.G.; Sanchez-Sutil, F. Enhanced Utility-scale Photovoltaic Units with Frequency Support Functions and Dynamic Grid Support for Transmission Systems. *IET Renew. Power Gener.* **2017**, *11*, 361–372. [[CrossRef](#)]
2. Bueno, P.G.; Hernández, J.C.; Ruiz-Rodriguez, F.J. Stability Assessment for Transmission Systems with Large Utility-scale Photovoltaic Units. *IET Renew. Power Gener.* **2016**, *10*, 584–597. [[CrossRef](#)]
3. Li, H.; Shang, J.; Zhang, B.; Zhao, X.; Tan, N.; Liu, C. Stability Analysis With Considering the Transition Interval for PWM DC-DC Converters Based on Describing Function Method. *IEEE Access* **2018**, *6*, 48113–48124. [[CrossRef](#)]
4. Li, J.; Lee, F.C. Modeling of V^2 Current-Mode Control. *IEEE Trans. Circuits Syst. I Regul. Pap.* **2010**, *57*, 2552–2563. [[CrossRef](#)]
5. Zhao, C.; Round, S.D.; Kolar, J.W. Full-Order Averaging Modelling of Zero-Voltage-Switching Phase-Shift Bidirectional DC-DC Converters. *IET Power Electron.* **2010**, *3*, 400–410. [[CrossRef](#)]
6. Surya, S.; Williamson, S. Generalized Circuit Averaging Technique for Two-Switch PWM DC-DC Converters in CCM. *Electronics* **2021**, *10*, 392. [[CrossRef](#)]
7. Azer, P.; Emadi, A. Generalized State Space Average Model for Multi-Phase Interleaved Buck, Boost and Buck-Boost DC-DC Converters: Transient, Steady-State and Switching Dynamics. *IEEE Access* **2020**, *8*, 77735–77745. [[CrossRef](#)]
8. Middlebrook, R.D.; Čuk, S. A General Unified Approach to Modelling Switching-Converter Power Stages. *Int. J. Electron.* **1977**, *42*, 521–550. [[CrossRef](#)]
9. Wang, X.; Zhuo, F.; Li, J.; Wang, L.; Ni, S. Modeling and Control of Dual-Stage High-Power Multifunctional PV System in d-Q-o Coordinate. *IEEE Trans. Ind. Electron.* **2013**, *60*, 1556–1570. [[CrossRef](#)]
10. Wang, Q.; Yao, W.; Fang, J.; Ai, X.; Wen, J.; Yang, X.; Xie, H.; Huang, X. Dynamic Modeling and Small Signal Stability Analysis of Distributed Photovoltaic Grid-Connected System with Large Scale of Panel Level DC Optimizers. *Appl. Energy* **2020**, *259*, 114132. [[CrossRef](#)]
11. Rasheduzzaman, M.; Mueller, J.A.; Kimball, J.W. An Accurate Small-Signal Model of Inverter-Dominated Islanded Microgrids Using d-q Reference Frame. *IEEE J. Emerg. Sel. Top. Power Electron.* **2014**, *2*, 1070–1080. [[CrossRef](#)]
12. Emadi, A. Modeling and Analysis of Multiconverter DC Power Electronic Systems Using the Generalized State-Space Averaging Method. *IEEE Trans. Ind. Electron.* **2004**, *51*, 661–668. [[CrossRef](#)]
13. Liu, X.; Cramer, A.M.; Pan, F. Generalized Average Method for Time-Invariant Modeling of Inverters. *IEEE Trans. Circuits Syst. I Regul. Pap.* **2017**, *64*, 740–751. [[CrossRef](#)]
14. Wang, Y.; Wang, X.; Chen, Z.; Blaabjerg, F. Small-Signal Stability Analysis of Inverter-Fed Power Systems Using Component Connection Method. *IEEE Trans. Smart Grid* **2018**, *9*, 5301–5310. [[CrossRef](#)]
15. Wang, Y.; Wang, X.; Blaabjerg, F.; Chen, Z. Harmonic Instability Assessment Using State-Space Modeling and Participation Analysis in Inverter-Fed Power Systems. *IEEE Trans. Ind. Electron.* **2017**, *64*, 806–816. [[CrossRef](#)]
16. Sampaio, L.P.; de Brito, M.A.G.; e Melo, G.D.A.; Canesin, C.A. Grid-Tie Three-Phase Inverter with Active Power Injection and Reactive Power Compensation. *Renew. Energy* **2016**, *85*, 854–864. [[CrossRef](#)]
17. Dehghanzadeh, A.; Farahani, G.; Maboodi, M. A Novel Approximate Explicit Double-Diode Model of Solar Cells for Use in Simulation Studies. *Renew. Energy* **2017**, *103*, 468–477. [[CrossRef](#)]
18. Mohammadi, M.; Hamedani, B.; Hatami, S. An Accurate and Fast Piece-Wise Linear Approach for Real-Time Simulation of PV Arrays Under Non-Uniform Condition. In Proceedings of the 34th International Power System Conference (psc2019), Tehran, Iran, 9–11 December 2019; IEEE: New York, NY, USA, 2019; pp. 662–665.
19. Theocharis, A.D.; Pyrgioti, E.C. Development of a Linearized Photovoltaic Generator Model for Simulation Studies with Electromagnetic Transient Programs. *Int. Trans. Electr. Energy Syst.* **2015**, *25*, 454–470. [[CrossRef](#)]
20. Villalva, M.G.; de Siqueira, T.G.; Ruppert, E. Voltage Regulation of Photovoltaic Arrays: Small-Signal Analysis and Control Design. *IET Power Electron.* **2010**, *3*, 869–880. [[CrossRef](#)]
21. Li, S. Linear Equivalent Models at the Maximum Power Point Based on Variable Weather Parameters for Photovoltaic Cell. *Appl. Energy* **2016**, *182*, 94–104. [[CrossRef](#)]
22. Lekshmi Sree, B.; Umamaheswari, M.G. A Hankel Matrix Reduced Order SEPIC Model for Simplified Voltage Control Optimization and MPPT. *Sol. Energy* **2018**, *170*, 280–292. [[CrossRef](#)]
23. Durgadevi, S.; Umamaheswari, M.G. Analysis and Design of Single-Phase Power Factor Corrector with Genetic Algorithm and Adaptive Neuro-Fuzzy-Based Sliding Mode Controller Using DC-DC SEPIC. *Neural Comput. Appl.* **2019**, *31*, 6129–6140. [[CrossRef](#)]
24. Prajapati, A.K.; Prasad, R. Model Order Reduction by Using the Balanced Truncation and Factor Division Methods. *IETE J. Res.* **2019**, *65*, 827–842. [[CrossRef](#)]
25. Zhang, M.; Miao, Z.; Fan, L. Reduced-Order Analytical Models of Grid-Connected Solar Photovoltaic Systems for Low-Frequency Oscillation Analysis. *IEEE Trans. Sustain. Energy* **2021**, *12*, 1662–1671. [[CrossRef](#)]
26. Anand, S.; Fernandes, B.G. Reduced-Order Model and Stability Analysis of Low-Voltage DC Microgrid. *IEEE Trans. Ind. Electron.* **2013**, *60*, 5040–5049. [[CrossRef](#)]
27. Rasheduzzaman, M.; Mueller, J.A.; Kimball, J.W. Reduced-Order Small-Signal Model of Microgrid Systems. *IEEE Trans. Sustain. Energy* **2015**, *6*, 1292–1305. [[CrossRef](#)]
28. Wang, J.; Yan, J.D.; Jiang, L.; Zou, J. Delay-Dependent Stability of Single-Loop Controlled Grid-Connected Inverters with LCL Filters. *IEEE Trans. Power Electron.* **2016**, *31*, 743–757. [[CrossRef](#)]

29. Fischer, J.R.; González, S.A.; Herrán, M.A.; Judewicz, M.G.; Carrica, D.O. Calculation-Delay Tolerant Predictive Current Controller for Three-Phase Inverters. *IEEE Trans. Ind. Inform.* **2014**, *10*, 233–242. [[CrossRef](#)]
30. Lyu, Y.; Lin, H.; Cui, Y. Stability Analysis of Digitally Controlled LCL-Type Grid-Connected Inverter Considering the Delay Effect. *IET Power Electron.* **2015**, *8*, 1651–1660. [[CrossRef](#)]
31. Barmada, S.; Formisano, A.; Hernandez, J.C.; Sánchez Sutil, F.J.J.; Petrarca, C. Impact of Nearby Lightning on Photovoltaic Modules Converters. *COMPEL—Int. J. Comput. Math. Electr. Electron. Eng.* **2021**, *41*, 628–643. [[CrossRef](#)]
32. Garcia, O. Guidelines for Protection against Overcurrent in Photovoltaic Generators. *Adv. Electr. Comp. Eng.* **2012**, *12*, 63–70. [[CrossRef](#)]
33. García, O.G.; Hernández, J.C.; Jurado, F. Assessment of Shading Effects in Photovoltaic Modules. In Proceedings of the 2011 Asia-Pacific Power and Energy Engineering Conference, Wuhan, China, 25–28 March 2011; pp. 1–4.
34. Zhang, Z.; Mishra, Y.; Yue, D.; Dou, C.; Zhang, B.; Tian, Y.-C. Delay-Tolerant Predictive Power Compensation Control for Photovoltaic Voltage Regulation. *IEEE Trans. Ind. Inform.* **2021**, *17*, 4545–4554. [[CrossRef](#)]
35. Zhang, X.; Spencer, J.W.; Guerrero, J.M. Small-Signal Modeling of Digitally Controlled Grid-Connected Inverters With LCL Filters. *IEEE Trans. Ind. Electron.* **2013**, *60*, 3752–3765. [[CrossRef](#)]
36. Li, S. A Variable-Weather-Parameter MPPT Control Strategy Based on MPPT Constraint Conditions of PV System with Inverter. *Energy Convers. Manag.* **2019**, *197*, 111873. [[CrossRef](#)]
37. Li, S. A Maximum Power Point Tracking Method with Variable Weather Parameters Based on Input Resistance for Photovoltaic System. *Energy Convers. Manag.* **2015**, *106*, 290–299. [[CrossRef](#)]
38. Li, S.; Ping, A.; Liu, Y.; Ma, X.; Li, C. A Variable-Weather-Parameter MPPT Method Based on a Defined Characteristic Resistance of Photovoltaic Cell. *Sol. Energy* **2020**, *199*, 673–684. [[CrossRef](#)]
39. Liu, J.; Molinas, M. Impact of Inverter Digital Time Delay on the Harmonic Characteristics of Grid-Connected Large-Scale Photovoltaic System. *IET Renew. Power Gener.* **2020**, *14*, 3809–3815. [[CrossRef](#)]
40. Wu, T.-F.; Chen, Y.-K. Modeling PWM DC/DC Converters out of Basic Converter Units. *IEEE Trans. Power Electron.* **1998**, *13*, 870–881. [[CrossRef](#)]
41. Li, S.; Li, Q.; Qi, W.; Chen, K.; Ai, Q.; Ma, X. Two Variable-Weather-Parameter Models and Linear Equivalent Models Expressed by Them for Photovoltaic Cell. *IEEE Access* **2020**, *8*, 184885–184900. [[CrossRef](#)]
42. Bryant, B.; Kazimierczuk, M.K. Voltage-Loop Power-Stage Transfer Functions With MOSFET Delay for Boost PWM Converter Operating in CCM. *IEEE Trans. Ind. Electron.* **2007**, *54*, 347–353. [[CrossRef](#)]
43. Golestan, S.; Guerrero, J.M.; Vidal, A.; Yepes, A.G.; Doval-Gandoy, J.; Freijedo, F.D. Small-Signal Modeling, Stability Analysis and Design Optimization of Single-Phase Delay-Based PLLs. *IEEE Trans. Power Electron.* **2016**, *31*, 3517–3527. [[CrossRef](#)]
44. Hutton, M.; Friedland, B. Routh Approximations for Reducing Order of Linear, Time-Invariant Systems. *IEEE Trans. Autom. Control* **1975**, *20*, 329–337. [[CrossRef](#)]

Disclaimer/Publisher’s Note: The statements, opinions and data contained in all publications are solely those of the individual author(s) and contributor(s) and not of MDPI and/or the editor(s). MDPI and/or the editor(s) disclaim responsibility for any injury to people or property resulting from any ideas, methods, instructions or products referred to in the content.